Radiation Effects on Mechanical Properties of Thin 3C-SiC Investigated by *in situ* Nanoindentation *via* Transmission Electron Microscopy

By
Xuying Liu

A dissertation submitted in partial fulfillment of
the requirements for the degree of

Doctor of Philosophy
(Materials Science and Engineering)

at the
UNIVERSITY OF WISCONSIN – MADISON
2020

Date of final oral examination: 12/17/2019

The dissertation is approved by the following of the Final Oral Committee:
Paul Voyles, Professor, Materials Science and Engineering
Izabela Szlufarska, Professor, Materials Science and Engineering
Don Stone, Professor, Materials Science and Engineering
Melih Eriten, Associate Professor, Mechanical Engineering
Adrien Couet, Assistant Professor, Engineering Physics

Acknowledgements

I would like to express my sincere appreciation to my advisor Professor Paul Voyles, for his time, guidance, encouragement, and trust, without which this work would not have been possible. I am truly grateful for his support on my research and his willingness to offer useful advice all the time. I am also thankful to all my committee members for providing insights to my research project and thesis. Particularly, I would like to thank Professor Izabela Szlufarska for the help all through the whole project as a collaborator, and Professor Don Stone for the discussion about dislocation movement and mechanical property of ceramics. Additionally, thanks so much for the discussion from Professor Melih Eriten on *ex situ* nanoindentation data analysis, and for the really useful and important courses I took from Professor Adrien Couet about nuclear materials and radiation damage.

I want to express my thanks to all current and former group members: Chenyu Zhang, Sachin Muley, Debaditya Chatterjee, Carter Francis, Jingrui Wei, John Sunderland, Shuoyuan Huang, Pei Zhang, Congli Sun, Jie Feng, Jason Maldonis, Dan Zhou, Li He, and Ashutosh Rath. I am in a group with kind, diligent, enthusiastic and creative colleagues and at the same time friends. Thank you all for the help both academically and personally. I would also thank to all my collaborators Chaiyapat Tangpatjaroen, Cheng Liu, Xing Wang from Professor Izabela Szlufarska's group and Shuaifang Zhang from Professor Michael Tonks' group. I am thankful to Alex Kvit, Rick Noll and all other staffs of the labs for equipment training and support.

I also want to say thank you to my parents for wavering support and understanding, and to my fiancé Tristan Brown for his love and support to me in both good times and bad times. I could not have accomplished my research or my degree without all your help.

Abstract

In situ nanoindentation tests on thin 3C-SiC in a transmission electron microscope (TEM) show small but non-negligible plastic deformation at room temperature. SiC is brittle in macroscopic studies but it can be become ductile when deformation occurs in small volumes. We report a brittle to ductile transition of 3C-SiC during nanoindentation of thin films (150-270 nm thick) and we reveal mechanisms of plastic deformation *in situ*. We found that plasticity in 3C-SiC is driven by dislocations and that there is a pronounced plastic strain recovery at these length scales. We suggest that plastic deformation recovery arises from annihilation of transient dislocation extension driven by retracted external stress. In addition, we discovered that when the sample thickness decreases to less than 90 nm, 3C-SiC becomes brittle again, showing that the thickness of the films is important in determining whether the sample is brittle or ductile.

In situ TEM nanoindentation tests on thin 3C-SiC irradiated at different radiation conditions indicate different mechanical behavior that is related to different microstructures. Samples irradiated at 600 °C 0.3 dpa and 600 °C 3 dpa are easier to fracture under applied force than as-synthesized 3C-SiC. Long, straight, and simple crack paths are characteristic features for 600 °C 3 dpa samples, which is an evidence of easier fracture than 600 °C 0.3 dpa. However, 900 °C 3 dpa samples do not exhibit noticeable brittleness. Instead, they exhibit plastic deformation under applied force, which is the same as as-synthesized samples. Based on the microstructure of the irradiated samples, increasing the density of black spot defects that form at 600 °C degrades resistance to cracking, but the change of defect type to dislocation loops at 900 °C restores the plastic behavior.

The results from this study are not consistent with macroscale analysis of fracture and cracking in irradiated SiC, which suggest different behavior and the microscale in irradiated as well as unirradiated SiC. These results therefore provide useful insights into the microscale properties of 3C-SiC which are important to multiscale simulation of 3C-SiC to predict mechanical performance of microelectromechanical systems, coatings, and next-generation fission reactor fuels.

Table of contents

List of figures

List of tables

Chapter 1 Introduction of 3C-SiC

1.1 Polytypes of SiC and structures

There have been more than 250 polytypes of SiC reported so far according to varied atomic stacking sequences of closed-packed Si-C planes [1]. All different crystal structures have the same composition of 50% Si atoms and 50% C atoms covalently bounded as tetrahedral coordination, i.e. each Si atom's nearest neighbors consist of four C atoms, or the opposite. The most common polytypes are 2H, 4H, 3C, 6H, and 15R, in which the number refers to numbers of layers needed for repetition and H, C, R represent hexagonal, cubic and rhombohedral [2]. Among all these polytypes, only 4H-SiC, 6H-SiC and 3C-SiC are commercially available and have been explored to serve in electronic devices and circuits, such as semiconductors, sensors, microelectromechanical systems (MEMS)/nanoelectromechanical systems (NEMS), and nuclear reactors, which will be explained in the following part of the chapter.

3C-SiC, also called Beta-SiC (β-SiC), is the only polytype among myriad variations that has isotropic cubic symmetry. 4H-SiC, 6H-SiC, and other non-cubic (mostly accepted as hexagonal) structured polytypes are called alpha-SiC (α-SiC). More specific cubic structure of 3C-SiC is zinc blende structure belonging to space group $F\bar{4}3m$ [3]. It means that it is face-centered cubic crystal structure, with 4-fold rotoinversion along c-axis, 3-fold rotation along <111> directions and {110} mirror planes. The elements Wyckoff IDs and positions are Si 4a, 0 0 0, and C 4c, ¼ ¼ ¼. Compared with anisotropic behavior in properties of hexagonal polytypes, 3C-SiC exhibits isotropic behavior in many aspects due to its cubic crystal structure, which makes it stand out from other popular polytypes.

The current methods to fabricate SiC are sintering, direct conversion, chemical vapor deposition (CVD), pyrolysis, and so on [2]. CVD, the way how our samples were fabricated, is a popular gas phase reaction to create high density, high purity and highly oriented 3C-SiC [4]. The diagram in Ref [5] indicates a peritectic transition temperature 2545 ± 40 °C as the most reliable decomposition temperature so far. Density of 3C-SiC is 3.21g/cm^3, and lattice constant is 4.36 Å at room temperature derived from X-ray diffraction [5].

1.2 Properties of 3C-SiC

1.2.1 Electric properties

SiC is commonly considered as a wide bandgap material, due to its high energy bandgap (2.3-3.2) eV, and high breakdown field (1.8-4) MV/cm [6][7]. SiC also has higher saturated electron velocity (2-2.5) × 10^7 cm/s, which is a good for high-frequency applications and handle higher power density than Si or GaAs. 3C-SiC has larger bandgap 2.3 eV and higher breakdown field 1.8 MV/cm, while bandgap and breakdown field of Si are 1.1eV and 0.6MV/cm. Furthermore, 3C-SiC has relatively high electron mobility 750 cm^2/(V•S) among varied polytypes [8]. Since 4H-SiC and 6H-SiC are commercially available in the single crystal wafer form by epitaxial growth, with smoother surface and fewer defects than 3C-SiC, semiconductor, n-type, p-type, and semi-insulating hexagonal SiC wafers are popular in the market [6]. However, 3C-SiC is the only polytype that can heteroepitaxially grown on non-SiC substrate with huge opportunity to reach the required thickness for specific application [9][10]. Thus, 3C-SiC is primarily considered to serve in MEMS.

1.2.2 Thermal properties

The stability of SiC mostly depends on temperature, and it is believed that 3C-SiC is the preferred polytype than 6H-SiC under the peritectic transition temperature [11]. Since other hexagonal polytypes have simpler stacking sequences, they are not expected to exist under high temperature. Therefore, 3C-SiC is supposed to be the most stable polytype between room temperature and 2373 K. Other conditions, for example, impurities, applied force, radiation, can also trigger phase transformation among different polytypes, even amorphization.

Thermal conductivity is a measure of ability to conduct heat and SiC is considered as a ceramic having relatively high thermal conductivity at relatively low temperatures. In general, values of thermal conductivity of all kinds of SiC reach a peak around 200 K and decrease as temperatures increase until nearly constant, for example in the figure of the summary of 3C-SiC in Ref [2]. Around room temperature (~300K), CVD polycrystalline 3C-SiC with grain size <10μm is reported to have thermal conductivity ~360 W/mK, which is close to pure dense single crystal SiC that has the highest thermal conductivity among all kinds of SiC [2][12]. Thermal conductivity also depends on grain size [12] and grain boundary properties [2].

Thermal expansion is the result of increasing interatomic spacing between atoms of SiC with increasing temperature. Due to the strong covalent bonding, SiC has comparatively low thermal expansion and small coefficient. However, the magnitude of SiC thermal expansion is highly crystal structure dependent [2]. For hollow semispherical 3C-SiC shells for nuclear plant application from 300 K to 800 K, interferometric method measured the coefficient about $4.38*10^{-6}$ K^{-1}.

1.2.3 Mechanical properties

SiC fabricated in different methods will have different grain size, density, cystography, which will exhibit different mechanical properties. Based on the research, the summary of mechanical properties here will only about polycrystalline CVD SiC materials.

Elastic modulus or Young's modulus is one of the most important mechanical properties that represents the material's resistance to being deformed elastically. At room temperature, bulk 3C-SiC elastic modulus were measured to be (430-500) GPa by Vickers indentation [13], four-point bend flexural testing [14], and nanoindentation tests [15][16]. For thin-film 3C-SiC, elastic modulus measurement methods are various, besides nanoindentation[17][18], load-deflection tests [19] and micro-tensile [20][21] tests were also applied to obtain modulus (360-450) GPa. Moreover, compression tests on micropillar with 0.65μm diameter result in 465 GPa elastic modulus [22]. Temperature [14] and porosity [23] has effects on elastic modulus and the following other mechanical properties under specific conditions.

Hardness is a mechanical property related to both elastic deformation and plastic deformation, as well as fracture and toughness. SiC is known as a hard material and bulk 3C-SiC has hardness (35-40) GPa by nanoindentation tests [15][16], while ~21 GPa Vickers hardness [13]. Hardness of 3C-SiC films on Si substrates for MEMS/NEMS has been measured to be ~32 GPa [17][18]. Temperature has a huge effect on hardness which is reflected on the ductile-to-brittle transition (DBT) curve, in which hardness is nearly constant below DBT temperature, and rapidly decreases with increasing temperature. However, DBT temperature varies on experimental conditions, for example in Ref [23], DBT temperature during indentation is lower than during tensile or bending tests. More discussion about hardness and DBT temperature and how they are related to other mechanical properties and experimental results will be mentioned in following chapters.

Poisson's ration of CVD polycrystalline 3C-SiC is reported to be ~0.18 for bulk materials by nanoindentation tests [15], and ~0.24 for thin-film 3C-SiC via micro-tensile tests [21] and calculation from load-deflection results [19]. Shear modulus was measured by four-point bend flexural testing to be 191 GPa [14] and shear strength has been reported to be (5-7) GPa by the micropillar compression tests [22].

Fracture toughness is crucial due to the fact that SiC is a brittle ceramic material, and fracture toughness is a quantitative way to indicate the resistance to brittle fracture when a crack is present. High fracture toughness means more difficult or requiring more energy to fracture. For bulk CVD polycrystalline 3C-SiC, reported fracture toughness values are scattered from 2 MPa•m$^{1/2}$ to 5 MPa•m$^{1/2}$. Conventional Vickers indentation [2] and Chevron notched beam [2] methods lead to ~3.3 MPa•m$^{1/2}$ fracture toughness, three or four-point bending tests show a broad range (2-4.7) MPa•m$^{1/2}$ [24], and microindentation tests reveal fracture toughness ~2.8 MPa•m$^{1/2}$ [16]. However, the value of fracture toughness of thin-film 3C-SiC in Ref [18] 4.6 MPa•m$^{1/2}$ falls in the range of bulk 3C-SiC, while Ref [17] claims that thin film material has a much lower fracture toughness ~1.5 MPa•m$^{1/2}$ than bulk material. This broad range of values are not surprising due to the complexity of brittle fracture and microcrack besides grain-size effects.

1.2.4 Chemical properties

Since the electronegativity of Si and C are different, the chemical bonding of SiC is not only covalent bond, but also slightly ionic bond. This is directly related to the thermal decomposition temperature and stability of SiC under high temperature, which have been discussed above.

At room temperature SiC is considered as non-oxide compound, however, under high temperature, high oxygen pressure, or wet environment, passive or active oxidation will happen. Under high temperature and high temperature, there is a mass gain from passive oxidation:

$SiC + 3/2\ O_2 \rightarrow SiO_2 + CO$

The rate of oxidation is controlled by diffusion: oxygen diffusion inward and CO diffusion outward. Jorgensen et al.'s study confirmed that in an atmosphere of dry oxygen between 900 °C to 1600 °C, oxidation resulted in amorphous silica or cristobalites depending on the temperature. Both will form oxide protective films [25]. According to the table in Ref [26] about the summary of all kinds of SiC passive oxidation in dry atmosphere, oxidation resistance of CVD SiC is superior to other kinds of SiC at high temperatures. Active oxidation will generate SiO without protective SiO_2:

$SiC + O_2 \rightarrow SiO + CO$

The active-to-passive oxidation of SiC is dependent on impurity content of SiC [2].

1.3 Application in Microelectromechanical Systems

Microelectromechanical systems and nanoelectromechanical systems are families of technologies that begins to make significant impact in modern life, such as medication, energy, instrumentation, transportation and so on [27]. SiC is an outstanding ceramic material for high-power, high-temperature, high-frequency electronics due to its high band gap, high breakdown field, high saturation electron velocity, and high electron mobility [6], which can play an important role in serving for MEMS and NEMS. Conventional high-load nanoindentation tests have been done on single crystal 3C-SiC films and polycrystalline 3C-SiC films, suggesting that poly-3C-SiC has higher hardness and modulus compared with single crystal 3C-SiC, as well as higher wear resistance [17]. Since polycrystalline 3C-SiC has better mechanical properties, it will be more suitable for MEMS/NEMS applications.

Some of already completed 3C-SiC-based microsystems are including resonators [28][29], nanocantilevers [30] and all kinds of sensors [31] (pictures of them can be found in references). For vertical resonators in Ref [29], the resonant frequencies and the quality factors are much higher than equivalent Si devices [32]. Nanocantilevers fabricated in Ref [30] are less sensitive to noise and allow preamplifiers to be installed at a longer distance without a huge degradation of the signal, which is really useful advantage for electric devices in vacuum. As well, 3C-SiC based MEMS/NEMS can solve the requirement of cooling systems or radiation shielding [9].

Although growing 3C-SiC in wafer form is more difficult than 4H or 6H-SiC, the potential to grow 3C-SiC on Si and other substrates still worth exploring. Epitaxial is possible with a 20% lattice parameter mismatch between Si and SiC, and 3C-SiC films grown on (100) Si wafers have less residual stress than films grown on (111) [18]. Even though films grown on (111) Si have better properties, they produce large bow and then fail because of fracture [18]. Therefore, to make 3C-SiC more applicable in MEMS/NEMS application with doping, implantation, defect controlling techniques, different 3C-SiC growth systems have been built. Mehran Mehregany et al. [33] have built a low pressure chemical vapor deposition furnace to grow large scale (6-inch) epitaxial 3C-

SiC on Si substrate. Due to the capability of growing on Si substrates, common Si micromachining techniques can be used to fabricate bulk micromachined 3C-SiC MEMS/NEMS structures [27], which makes 3C-SiC better to be suitable in electronic device applications.

1.4 Application in nuclear engineering

1.4.1 Next generation nuclear reactors

Nuclear energy is one of the clean energy resources that do not consuming traditional fossil fuels or generating carbon dioxide to the environment. Besides, it has higher energy efficiency compared with coal, natural gas. In the US, the light water reactors (LWRs) now in operation were designed and built back to the seventies, which was forty years ago. As the pressure of competing economic benefit from all new and ‘clean’ energy resources increases, the current reactors are reaching their limit burnup. Furthermore, more and more regulations have been created to safely guard the operation of those reactors. Therefore, new generation nuclear reactors are under development to meet the needs from economic benefit and safety concerns.

In the genealogy of large fission nuclear reactors, current LWRs in US belongs to Generation II and Generation II+ in Ref [34] Table 1. Current LWRs has two types, pressurized water reactors and boiling water reactors. Now the concerns from currently being operated reactors are: strain caused by swelling, internal pressurization, internal stress-corrosion fracture, coolant water induced external corrosion, and embrittlement [34]. From Generation III and Generation IV, reactors are completely new designs, and Generation IV nuclear reactors will be the next generation reactors that is under development. The most two popular types of new generation reactors are sodium fast reactors and very-high-temperature reactors (VHTR) [35] and both of them will use fast neutron energy.

The popular fuel design of VHTRs is tri-isotropic (TRISO)-layered particles that are firstly designed in Germany [34]. The structure and sizes of the fuel particle is labelled in the figure and it will be the heart of VHTRs. The sphere containing a kernel of Uranium fuel is surrounded by two CVD carbon layers and one CVD 3C-SiC layer in between. 3C-SiC will work as a barrier preventing fission product from leaking out, which is equivalent to cladding in current LWRs. Particles like the 1mm-diameter sphere will consist either a compact (cylinder) or pebbles (tennis balls) as the final fuel form.

To ensure the reliability of the spherical structure during service, mechanical properties of all parts of the design have been tried to or will be measured and tested. Hosemann et al. [36] specifically measured hardness and fracture toughness using nanoindentation and crushing tests. The results suggest that there is a hardness gradient in 3C-SiC layer where the outer edge exhibits higher hardness, and fracture toughness is much higher in the radial direction with transgranular cracks. High temperature mechanical behavior of 3C-SiC in TRISO particles have been investigated by Rohbeck et al. [37], indicating that disintegration of SiC layer occurred when temperature is higher than 2100 °C. A ton of models have been created to predict behavior of this certain structure[38], Davis et al. [39] claimed that the shell sphericity is the concerning factor to prevent accuracy of current models. Due to the special geometry and scale size, more measurements using different methods at scales should be done to further investigate mechanical properties of 3C-SiC under radiation.

1.4.2 Structural components

For some structural outer sheath design, SiC/SiC composites are used to be the materials for control rod sheath, central coupling tube, shear pins [40]. An alternative fission reactor application is SiC ceramic composite fuel cladding [40], and core structures in gas-cooled fast reactor [41]. More researches have been shifted to focus on engineering aspect of SiC composites in fission reactors, such as fabrication, joining, and evaluation.

Compared with fission reactors, fusion reactors have an advantage of not producing long-term radioactive waste. Since SiC-based composites have high heat capacity and high radiation resistance, they have been proposed to be structural material in fusion reactor since mid 1970s [40][42]. One of the most popular creation is SiC/SiC composites fusion blanket design [43], along with designs like first wall facing plasma, diverter interacting with edge plasma, flow channel insert application, and so on [42][41].

1.4.3 Goal of the Project

Idaho National Lab has been developing a finite element-based fuel performance code named BISON since 2008, which is written in a general way to be applied to all different fuels with variety of geometries [44]. Hales et al. has utilized TRISON code on analyzing performance of TRISO particles [45]. There are many models, for example PASTA, ATLAS, and TIMCOAT [38], that have been created to work on TRISON particle performance, however, all of them have different limitation and flaws that make it impossible to predict the fuel performance accurately enough.

The ultimate goal of the whole project is creating a multiscale framework that can be sued in BISON (Figure 1), which can provide mechanical failure of 3C-SiC in reactors.

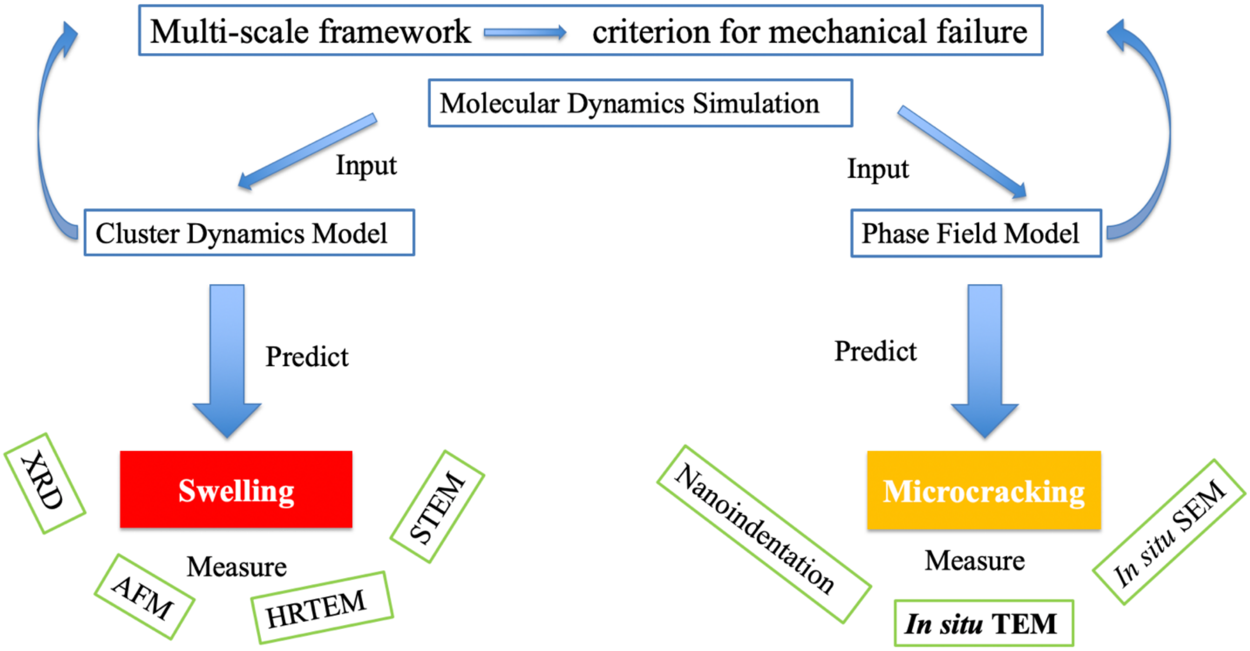

Figure 1 Project overview

My collaborators from two other groups are working on simulation and modelling. Molecular dynamic simulation (MD) is done by Professor Izabela Szlufarska's group, which generates inputs for both cluster dynamic model and phase field model. Cluster dynamic model has been built to successfully predict radiation induced defects size and density distribution under specific radiation condition, which is directly related to swelling [46]. Phase field model is being developed by Professor Michael Tonks' group, which can predict fracture behavior of 3C-SiC in a larger size scale. Meanwhile, swelling and microcracking behaviors can be measured and detected from experimental aspect. X-ray diffraction (XRD), atomic force microscopy (AFM) can measure how much the swelling is directly and using high resolution TEM (HRTEM) and scanning TEM

(STEM), small defects, such as black spot defects (BSD) and/or their clusters can be observed under atomic resolution [47]. In this study, *ex situ* nanoindentation tests, *in situ* nanoindentation tests in TEM have been performed to validate simulation results. The results will be shown in later chapters.

Chapter 2 Radiation Effect on 3C-SiC

2.1 Radiation damage

2.1.1 Displacement cascades during radiation

Scattering cross section represents the probability of occurrence of particular interaction between incident particle flux and atoms in materials. Regardless of transmutation, the first neutron-atom interaction is the formation of primary knock-on atom (PKA), in which incident particle, a neutron transfers kinetic energy to the PKA via a collision. The PKA becomes the energetic particle creating following displacement cascades. However, since electron density of much higher than nuclei, PKA will prefer transfer energy to elections as long as the transferred energy can be higher or equal to their ionization energy. After the energy of PKA is reduced so much that it is difficult to transfer energy to electrons, it will start to lose energy to nuclei and cause atoms to leave their original lattice positions. Those knocked atoms are called secondary knocked-on atoms and they will keep interacting with other atoms around and transfer kinetic energy until their energy is dissipated enough that it is smaller than the displacement energy of the atom, which is the termination of cascades. In this way, the microstructure of the material is changed directly resulting in the radiation damage.

Radiation will cause vacancies and interstitials due to missing of atoms at lattice positions and extra atoms in between lattice positions. However, those point defects will recombine or start to cluster creating dislocation loops and voids. Moreover, thermal migration will make all defects more mobile and precipitates will segregate along grain boundaries, as well generating He bubbles. The detailed change of microstructure of 3C-SiC will be introduced in the following part.

2.1.2 Ion radiation

Compared with neutron radiation, ions are changed particles, so they will interact a lot more with electrons than neutrons. Thus, neutrons will keep generating low-level radiation damage all along the radiation direction into the materials, while ions will generate a strongly peaked damage profile since after they start to interact with nuclei, they quickly lose their energies and stopped at a relatively short penetration depth (1-10 μm) [48].

This study is using carbon ions as incident particles to radiate 3C-SiC and there are several reasons why we use charged particle radiation in experimental studies. One of the advantages is much higher displacement rate than neutron radiation, for example, to reach 1dpa radiation damage, ion radiation will take hours while neutron radiation will take months [48]. Furthermore, ion-irradiated 3C-SiC is not as radioactive as neutron-irradiated samples, making samples easier to handle. However, one disadvantage is the short penetration depth and varying dose rate over penetration depth as mentioned before. Another drawback is lack of transmutation reaction in the procedure and shift of temperature during radiation [49].

2.2 Microstructure evolution of 3C-SiC under radiation

Without external force interference, at relatively low temperature with low radiation dose, amorphization of 3C-SiC has been investigated under heavy ion radiation, such as Kr [50], Xe [51] and even Si [52]. Wang et al. [50] observed amorphization in 3C-SiC irradiated at 100 °C and complete amorphization at 1.35 dpa dose, confirmed by high resolution TEM (RHTEM) and simulations. It is claimed that the amorphization is due to displacement cascade overlap and grain boundaries (GBs) enhance it. The enhanced amorphization along HBs could be explained by the possibility that GBs could increase the defect production rate, or amorphous phase might prefer nucleate at the GBs, or interstitial starvation around GBs. Bayu Aji et al. [51] have also observed denser collision cascades increasing the amorphization cross-section constant. The other mechanism for radiation induced amorphization mentioned by Weber et al. [52] is accumulated defect caused local energy and elastic instability.

However, as mentioned before, microstructure change due to radiation is dominated by defect generation and evolution below ~1500 °C. Quantitative synchrotron-based X-ray diffraction characterization and/with HRTEM or/and STEM become popular techniques to investigate microstructure evolution of 3C-SiC under radiation. The general trend of evolution has been revealed years ago in Ref [53], Ref [2], Ref [54] and Ref [55], and indicates regions in which different defects probably exist, but no exact boundaries. For example in Ref [2] Fig.17, besides amorphization, under low radiation temperatures and fluences, black spot defects (BSDs) and/or small loops are the main defects. BSDs are mostly tiny clusters of interstitials with various configurations that appear like nanoscale black spots in bright field TEM images [2][56]. Since BSD can have size smaller than 1 nm, it is difficult for conventional TEM to observe [46].

Tyburska-Püschel et al. [47] has used conventional TEM to observe BSDs and their clusters, and compared the results from synchrotron XRD analysis, the difference can be as high as 40% to 70%. However, in Ref [46] He et al. observed BSDs using STEM, which is quite consistent with XRD results. In the same paper, Liu et al. built a cluster dynamic model to predict small defect size and density distribution under certain radiation condition and is validated by the STEM experimental results. As temperature or/and radiation fluence increase, due to displacement cascade, small defects may evolve into dislocation loops even Frank loops which are the preferable configuration for clusters [57], since 3C-SiC has really low stacking fault energy, and both loops can be easily observed in TEM. At high temperature or/and high radiation fluence, defects are more likely to be dislocation network and voids.

2.3 Radiation-induced Swelling

One of the direct effects of microstructure on 3C-SiC is swelling and it is one of the crucial issues that engineers have to resolve before it can be applied to nuclear reactors. In Ref [58] Lin et al. measured the swelling of 3C-SiC irradiated up to 20 dpa from 400 °C to 1350 °C, and the swelling before 1000 °C can be as large as 2% based on the synchrotron based XRD, which is a direct evidence that swelling of 3C-SiC can be a crucial problem that needs to be investigated further.

Firstly, radiation-induced swelling of 3C-SiC is highly temperature dependent and the mechanism of swelling therefore also depends on the temperature, a comprehensive figure can be found in Ref [55] Figure 6. The point-defect swelling regime can be around 150 °C to 1000 °C [2] and the swelling is caused by lattice expansion induced isotropic volume expansion from radiation-induced point defects or/and their clusters. There are numerical synchrotron based XRD measurement showing the shift of peaks and increase of full width at half maximum (FWHM), which indicate the lattice expansion and change of defect types, and the results are consistent with observation under microscope up to 1 dpa [59]. At temperature below 1000 °C, a study shows that lattice expansion is due to homogeneous distribution of interstitial point defects that are not recovered and small defect clusters are mostly vacancy-rich [60]. However, molecular dynamic simulation used to investigate the impact of different point defect on swelling suggests that the Si and C vacancies contribution to swelling is noneligible based on the defect concentration, but there is no clear temperature dependence in the contribution of the defect concentration to swelling [61]. In general, within point-defect swelling regime, swelling decreases as temperature increases, which is attributed to defect recovery and recombination [47], since the mobility of vacancies and interstitials increase. Therefore, swelling around 1000 °C can have the lowest swelling as small as zero [62]. The other regime is cavity swelling regime and it can be higher than 1300 °C [63] and there is increase of swelling as temperature increases [63]. At temperature in between these two regimes, there is generation and evolution of Frank loops and dislocations that dominate the complex swelling behavior [63].

Secondly, swelling is related to radiation dose as well and there is a saturation of the dose under specific temperature [2]. The analysis from one XRD measurement exhibits that lattice expansion saturated after about 0.1 dpa in the temperature ranging from 380 °C to 1180 °C [64]. In the same literature, at high fluence ~30 dpa, density of dislocation loops increases dramatically and their contribution to swelling is non-negligible. Yano et al. [65] measured that at temperature between 450 °C and 650 °C, swelling decreases as fluence increases. However, at 1100 °C, measurements of irradiated 3C-SiC at 0.5 dpa and 1 dpa in Ref [62], swelling increases as fluence increases, which is consistent with trend shown in Ref [55] Figure 6 high temperature range.

2.3 Radiation effects on properties of 3C-SiC

2.4.1 Radiation induced change of elastic modulus and hardness

Yong's modulus and hardness have been measured on CVD polycrystalline 3C-SiC radiated under wide range of temperature and fluence. Nanoindentation tests, four-point bending tests, and Vickers indentation tests are the most popular methods. A comprehensive figure in Ref [2] shows some significant temperature dependent decrease of modulus with maximum 25%, after radiation below 1000 °C, which shares similar trend with point-defect swelling [2][15][55], but with a large scatter. Elastic modulus is determined by atomic bond strength, bond density, and atomic spacing [66], so it suggests that this decrease of modulus can be highly related to radiation-induced lattice expansion. However, radiation induced strain is reduced by high temperature effect, so the modulus decrease becomes negligible at temperature higher than 1000 °C [66]. Furthermore, there is no clear dependency of modulus on radiation fluence so far [15].

For metals, radiation can induce hardening by raising the stress required to initialize dislocation movement [49]. Measurement of irradiated 3C-SiC reveals less than 20% increase of hardness at temperature between 200 °C and 1200 °C [55], with no trend with temperature and small value scatter. Amorphization around 180 °C can cause decrease of hardness at small temperature range [67].

2.4.2 Radiation induced embrittlement

SiC is a brittle ceramic material, so brittle fracture is one of the most crucial issues. Fracture toughness represents how easy it is for a material to fracture and the measurement of a brittle material like SiC can vary significantly due to the lack of standardized experimental procedure and lack of comparable surface condition. Chevron notched beam technique, Vickers indentation and nanoindentation are the most common methods to measure fracture toughness of 3C-SiC. No matter Vickers indentation or/and nanoindentation tests, crack path measurement is used to calculate fracture toughness by mostly Evans–Davis model [68]. However, the methods to observe and measure crack path length can make results different, and that will lead to the scatter of fracture toughness values. Transgranular fracture surface of irradiated 3C-SiC has been observed *via* SEM and compared with unirradiated 3C-SiC fracture surface [15]. Fractography comparison shows that fracture surface of irradiated 3C-SiC has smaller flat cleavage surface area and cleavage surfaces are not as plain as unirradiated specimen, which has mirror-like clean large grain cleavage. Similar micro-crack paths of irradiated 3C-SiC from indentation tests have been observed by Park et al. [69], showing that after intermediate temperature radiation, 3C-SiC has very short crack path with complex crack propagation; while unirradiated 3C-SiC and high temperature irradiated 3C-SiC have linear long crack paths, which implies that higher energy is required to fracture after radiation.

In Ref [55][2][69][16], there can be a general trend of fracture toughness with change of temperature: below 400 °C, fracture toughness slightly decrease; a significant increase exists at 300 °C-1000 °C; almost no change of fracture toughness at high temperatures. The trends suggest that radiation-induced toughening can happen at intermediate radiation temperature, which rarely happen in metals under radiation. Fractography observation mentioned above in Ref [15][69] implies the cleavage resistance enhancement can be related to increase cleavage energy even toughening due to radiation. Lattice disorder due to microstructure evolution or damage accumulation can be one of the reasons to make crack pattern more complex [69]. Interaction with dislocation loops and small voids can also create impedance of crack propagation [70].

2.4.3 Radiation induced change of thermal conductivity

Thermal conductivities of 3C-SiC irradiated from 0.001 dpa to 10 dpa under temperature 80 °C-800 °C is summarized by Snead et al. [2]. It indicated that there is a huge decrease of thermal conductivity after radiation and the decrease impact is larger at higher fluence. Back to 1973, Price has measured thermal conductivity of fast neutron radiated 3C-SiC under 2.7 dpa-7.7 dpa and the results reveals that radiation under 550 °C reduced room-temperature conductivity by a factor of 9, while radiation under 1100 °C only reduced room-temperature conductivity by factor of 3, and grain size was not a key factor [71]. Snead later also proved that the thermal conductivity degradation of CVD polycrystalline 3C-SiC is more severe at lower temperature [72], which is consistent with the summarized plot figure in Ref [2].

For most ceramic materials like SiC, thermal conductivity is dominated by phonon scattering due to their low density of valence band electrons [55]. The decrease of thermal conductivity after radiation can be explain by the change of phonon mean free path caused by radiation-induced vacancy and interstitial defects. The trend of thermal conductivity is comparable to volume expansion and is a direct indictor that temperature reverse the radiation effects on both swelling and thermal conductivity degradation [71].

Chapter 3 Method: nanoindentation

3.1 Advantages of *in situ* (S)TEM

In situ (scanning) transmission electron microscope is becoming a more and more important technique to reveal live performance, functional mechanisms, synthetization, and reactions for complicated and nanoscale materials under certain conditions, for example, temperature, pressure, radiation, strain [73]. There are tons of fields of research that can take advantages of this technique currently or in the future, such as solid reactions which include heating, biasing, solid-state battery, solid-gas reactions including environment TEM and gas cells, and solid-liquid reactions including electrochemical liquid cell and photocatalytic liquid cell [74].

In general, there are several components of the *in situ* (S)TEM systems and all of them can be designed for the experiment requests. The holders for *in situ* (S)TEM are special holders equipped with specific transducer, or sensors with various functionalities to electrical, optical, mechanical and thermal control and measurements. For example, special windows on holders for liquid cell or gas cell experiments are made of SiN [75] and graphene [76] to ensure the abilities of observation, enclosure, reduction of beam damage [77]. Heating chips or wires have been implemented to *in situ* TEM heating holders, which allow temperature effects or thermal triggered reactions to be observed and measured simultaneously. However, there are a lot of limitation and challenges of heating up TEM specimens. One issue is sample bending when heated up, another one is sample stability during heating and other issues can be temperature range and heating rate [78]. The first indentation *in situ* TEM holder was invented in 1998 [79] and piezo control was used to control the movement of indenter. At that time, indentation tests were still without feedback of force/depth measurement.

The other parts of *in situ* (S)TEM systems are microscopes and data collection. The column off TEMs have been modified to make sure special holders and other cables can be equipped without causing vacuum and beam problems. Goniometers have to be redesigned on some microscopes to ensure the insertion of all kinds of *in situ* holders made by different manufactures. Ultra-fast cameras are installed to capture fast reactions and interactions. Video recording systems are implemented to work with cameras in order to take real time videos. Data collection can also include force/depth feedback and voltage or potential, temperature measurements. Nowadays, the development of this technique is reliable enough that useful data have been acquired and interesting videos or high-resolution pictures have been taken. However, there are still a lot of future developments that need to be done on the *in situ* (S)TEM systems, the latest review paper is Ref [73] Table 1. There are several aspects of problems that have already shown up in current research, such as how to minimize systematic artifacts and reliable methods to retrieve correlations between performance measurements and structural change. There is an example of how to obtain local and transient strain maps during *in situ* nanoindentation tests [80]. Since this field is really promising and under development, in the future the following aspects can be improved: higher spatial and temporal resolution, smaller drift even automagical correction, better data analysis systems to help understand the procedure, easier operation and less strict environment requirement [73].

The invention of coupling (S)TEM observation and indentation makes it possible to directly observe material dynamic performance at nanoscale through imaging and diffraction, and measure mechanical behavior at the same time [81]. *In situ* nanoindentation open a new era to observe microstructural evolution, defect annihilation, dislocation movement, grain boundary configuration, etc. in the most straightforward way, and acquire the mechanical behavior, for example, force and displacement curves, scratch depth simultaneously, making it easier to build the correlation between microstructural behavior and mechanical performance [82][83]. To make this happen, there was a history of the system setup from the *in situ* stage, to only qualitive observation [83], to acquire quantitative feedback from transducers [84]. Thanks to the MEMS/NEMS device, more sensors, actuators, circuits have been integrated to the *in situ* nanoindentation systems [84]. This has granted more accurate measurement to obtain meaningful stress-strain curves from force-displacement raw data and more sensitive detection of pop-in events.

However, there are also obvious disadvantages or flaw of the system. Most of the *in situ* nanoindentation holders are single-tilt or slightly double-tilt holders, which limit the observation angles and diffraction condition selection. Even though the movement of indenter controlled by piezo and transducer are as precise as it can be, there still exists coupled movement of different axis. Quantitative results from *in situ* nanoindentation tests can be not so comparable with *ex situ* nanoindentation tests. Explanation of sample behavior can be subjective and due to small volume and observation area, it is still a lot of argument about whether those results can represent material properties, considering size and surface effects.

3.2 *In situ* nanoindentation experiment setup

3.2.1 *In situ* TEM nanoindentation system

The experiments were performed in Nanoscale Imaging and Analysis Center of University of Wisconsin-Madison. The main TEM used for *in situ* nanoindentation tests are FEI TECNAI TF-30 300 keV TEM equipped with a CCD camera and a Gatan K2 camera, which can perform energy filtered TEM (EFTEM) and high angle angular dark field (HAADF) analysis. The image of this instrument is in Figure 2A. The *in situ* nanoindentation holder is Hysitron PI95 PicoIndenter (Figure 2B) with a cube corner tip that minimum diameter of the tip is 80 nm, as shown in Ref [85] Fig. 2.1 (c). For FEI compatible PI95 PicoIndenter, due to the narrow goniometer of the TEM, the transducer is directly connected to the indenter, as shown in Figure 2C. The metallic color left part is transducer and at the very end is the cube corner indenter. A stair-shaped Cu stage or sample mount is used to fix sample on the holder (Figure 2C right copper-color part with a screw). The thin sample is lifted out from the bulk material and then welded on the position with green box in Figure 2C on a wedge-shaped Si substrate (Figure 2D) and the side view shows the wedge shape with 1μm plateau on the top. Detailed thin sample preparation and sample geometry design will be exhibited in the next section.

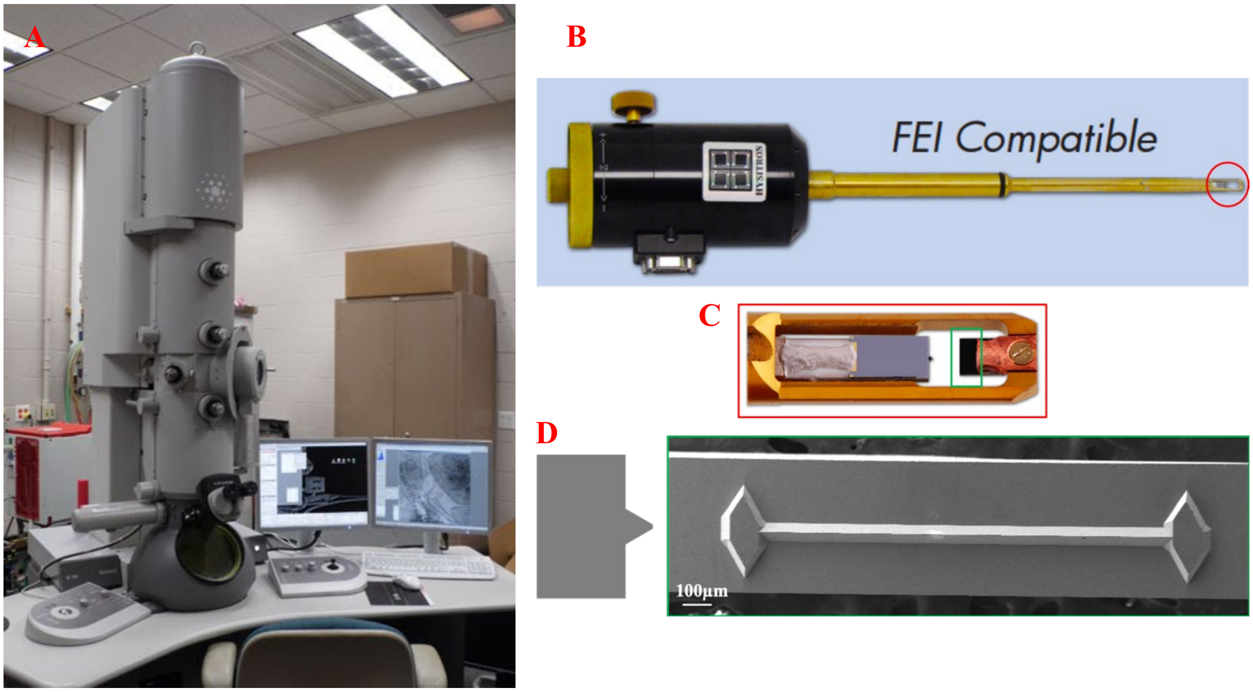

Figure 2 A is TF30 TEM. Hysitron PI95 PicoIndenter is B and the zoom-in of tip part is C. D shows Si wedge-shaped substrate and the side view of the substrate.

In situ nanoindentation tests were performed in Tecnai TF-30 TEM with the single tilt PicoIndenter holder operated in a displacement-controlled mode at a velocity of ~10 nm/s. Force-displacement curves and videos of indentation tests were obtained simultaneously. Videos were captured from a Gatan US1000 CCD camera at 15 frames per second. The thickness of the TEM samples was estimated by energy-filtered TEM following Ref [86] with a 3C-SiC inelastic mean free path under our acquisition condition of λ = 154 nm (details in Chapter 4). Characterization after indentation tests was done using TEM (Tecnai TF-30, 300 keV) and scanning electron microscopy (SEM, Zeiss/LEO 1530).

3.2.2 Bulk sample preparation

3C-SiC bulk samples (size 5 mm×5 mm×3 mm) were made by CVD (Rohm and Haas Company) and are polycrystalline with average grain size of 5 μm. Surfaces of small bulk samples were mechanically polished using diamond films with grades from 30 μm to 0.5 μm. More than 14 bulk samples were irradiated by carbon ions with energy of 5.15 MeV and flux about 5.5×10^{12} /cm^2/s in Ion Beam Lab of University of Wisconsin-Madison, and the rest of bulk samples were remained as synthesized. The radiated sample matrix with more detailed information is shown in Table 1 with temperatures 300 °C 600 °C 900 °C and radiation damage ranging from 0.06 dpa to 3 dpa. SRIM simulation of an 1dpa sample is shown in Figure 3. The unit dpa represents displacement per atom and the dpa for each sample is calculated based on the average dpa of first 1μm depth in SRIM-2013. Displacement energies of Si and C are 35 eV and 20 eV. The carbon radiation damage peak is around 3.5 μm depth for this study and the comparison with measurement from TEM observation will be mentioned later. The plateau range of radiation damage level until 2.5 μm can be used to mimic neutron radiation damage. Each bulk sample was cut into three 1.6 mm×5 mm×3 mm bulk samples using diamond saw (Allied High Tech Products, Inc. wafer blade with 4-inch in dimeter and 0.012-inch thickness) for *ex situ* nanoindentation and *in situ* nanoindentation usage.

Table 1 Irradiated sample matrix

300[°C]	600[°C]	900[°C]
	0.06 dpa	
	0.3 dpa	
0.6 dpa	0.6 dpa	0.6 dpa
	3 dpa	3 dpa

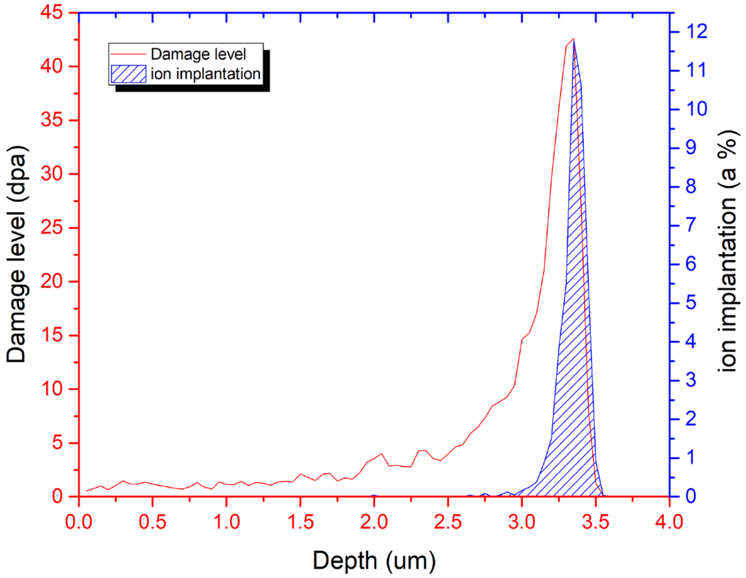

Figure 3 SRIM simulation of 5.15 MeV carbon ion radiation of 1 dpa sample

3.2.3 *In situ* nanoindentation sample geometry design and fabrication

Standard TEM samples were fabricated using focused ion beam (FIB, Zeiss Auriga) with 5 keV / 100 pA as the last polishing step to a final sample thickness of less than 100 nm. Standard FIB-made samples were analyzed in TEM (Tecnai TF-30, 300 keV) to characterize the as-synthesized microstructures of the material.

Irradiated bulk samples were flipped 90° to make radiation surfaces face to the side before FIB cutting. Sample for *in situ* indentation tests started with a piece of about 1.5 μm in thickness shown in Figure 4A (with lateral dimensions of 15 μm × 5 μm), and radiation damage depth zero side is at the edge. The piece was lifted out from the bulk material using an Omniprobe micromanipulator in the FIB with welding attachment on the non-irradiated area, as is shown in Figure 4B. The pieces were then welded on top of Si wedge-shaped substrates (Hysitron wide silicon wedge, 1 μm plateau) shown in Figure 4C-D with bottom welded. The alignment of 1.5 μm lift-out piece and 1 μm wedge plateau has to be very precise to the center of both (Figure D) in order to ensure the attachment and support (Figure 4E). A marker was milled near the radiation damage zero side to mark the radiation direction. Then it was thinned down to ~150 nm with 5 keV / 100 pA as the last polishing in FIB. Ar ion nanomilling (Fischione 1040 TEM Ion Mill) with 900 eV or Plasma FIB (FEI Helios G4) with 8 keV 100 pA was used as a final polishing step before indentation in order to reduce the amorphous layer created by Ga ion damage to less than 12 nm. Si substrate with sample was glued on the copper stair-shaped sample mount that was fixed on the holder (Figure 2C) using silver paint (Pelco Conductive, Ted Pella, Inc) and wait overnight before inserted to TEM for observation and testing.

An example of how the final *in situ* nanoindentation sample looks like in TEM before testing is Figure 5. This is a sample irradiated under 600 °C with damage level 0.3 dpa. The dark band in bright-field TEM image indicates the position of radiation damage peak, and the measurement of TEM is ~3.6 μm, which is consistent with SRIM simulation result ~3.5 μm in Figure 3. By this design of sample geometry and fabrication, the zero-radiation damage side is preserved and along the indenter force direction, the radiation damage level is supposed to be the same. The advantage is that the indentation condition is so well controlled that the corresponding radiation damage level for each indentation test can be accurately calculated.

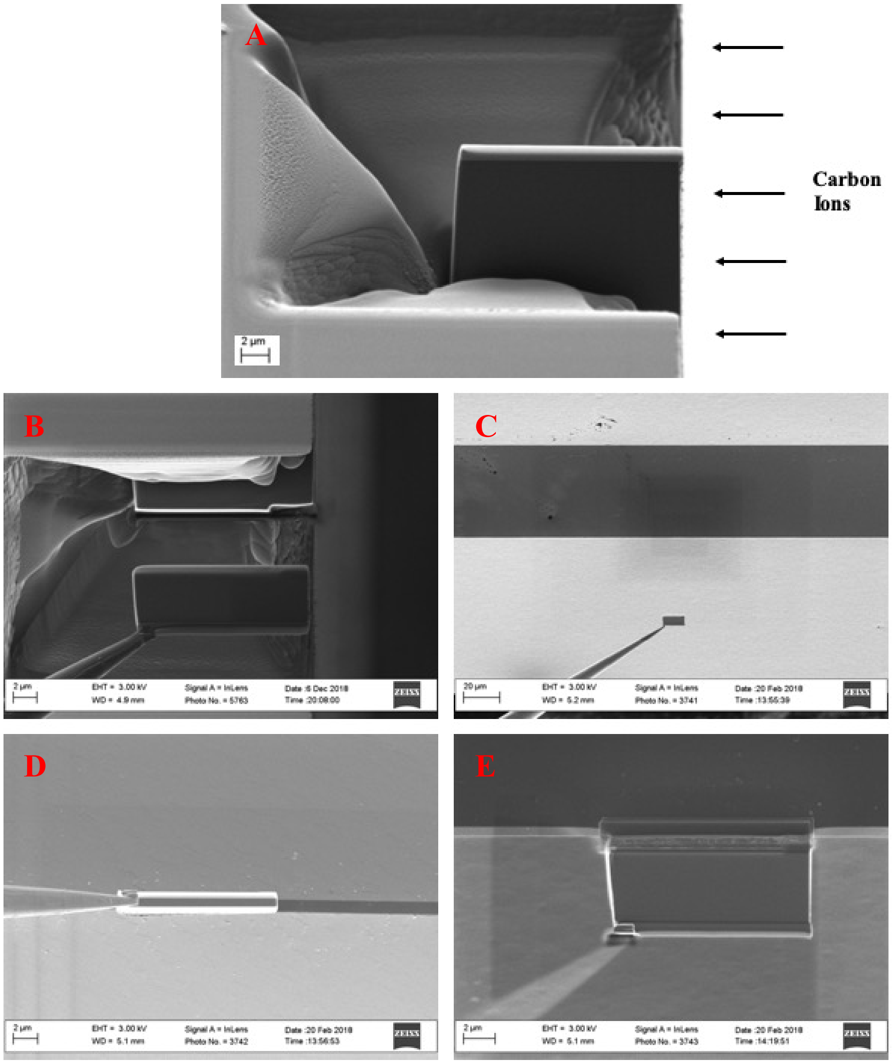

Figure 4 *In situ* nanoindentation sample preparation procedure using FIB

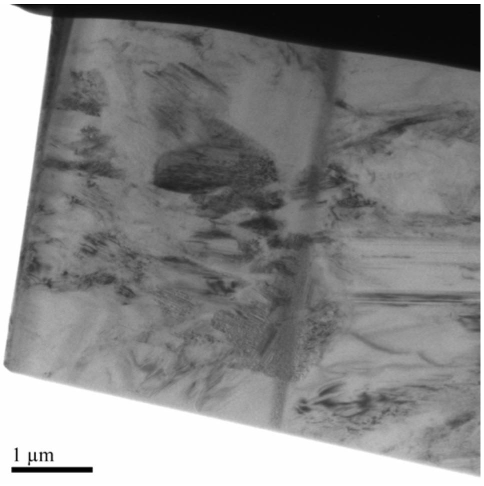

Figure 5 Bright-field TEM image of an *in situ* nanoindentation sample before testing

3.2.4 Examples of *in situ* nanoindentation tests with standard figure format

Most of my results from *in situ* nanoindentation tests are videos, and Figure 6 shows an example of how they are illustrated as image sequences with corresponding points on the load-displacement curves. Most of the results in Chapter 4 and Chapter 5 will follow the same figure format as Figure 6. The first image is load-displacement curve and the following images are sequences from *in situ* video, and they are labelled in correspondingly in the curve. Top part of sequence is always sample, and bottom part is the indenter.

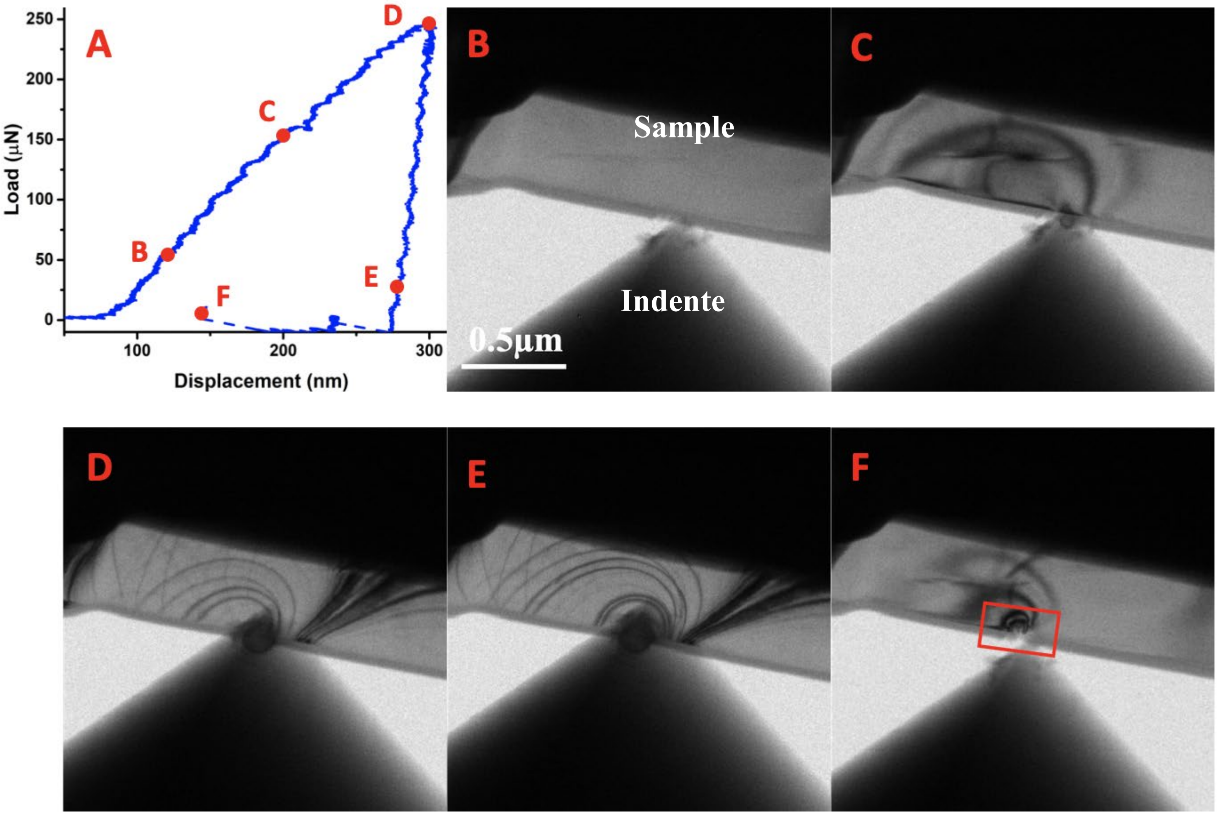

Figure 6 Example of *in situ* nanoindentation standard figure format

3.3 *Ex situ* nanoindentation experiment setup

Ex situ nanoindentation tests on bulk as-synthesized 3C-SiC and irradiated 3C-SiC were performed using a TriboIndenter (Hysitron TI 950, shown in Figure 7A) with a Berkovich tip. Figure 7B shows the geometry of the indenter tip and Figure 7C is the imprint geometry for the tip. Projected contact areas were measured in a SEM (Zeiss LEO 1530) to ensure accuracy.

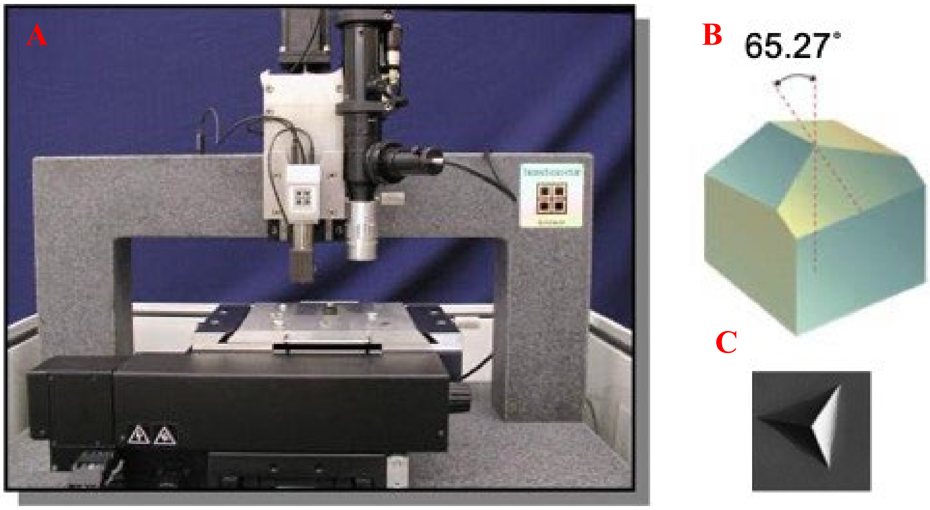

Figure 7 *Ex situ* nanoindentation test equipment illustration

Ex situ nanoindentation tests on irradiated samples were set up the way in Figure 8. The radiation surface is flipped to face the side so that the radiation damage depth is from the edge to inside to the 3.6 μm position and the radiation damage level is the same along the indenter force direction. In this way, the radiation effected depth does not to be treated as thin film on top of non-irradiated substrate and substrate effect can be avoided. However, since the damage depth is only 3.6 μm, and the indentation was done along the edge, edge effect has to be considered. To investigate radiation effects on mechanical properties of 3C-SiC and due to the ion radiation damage level condition, indenting at different damage depth can consider any difference of mechanical properties due to potentially change of radiation damage level. As in Figure 8A, the edge representing zero radiation damage was rotated about 2° to make the 30 indents separated 3μm cover 3 μm depth away from the edge as shown in Figure 8B. Scanning images with size of 10 μm × 10 μm by the indenter were required after each 10 indents (Figure 8C) and distance from the edge can be measured. To compare change of mechanical properties caused by radiation effects, same set of indentation was performed on the same bulk sample during the same experimental session to minimize random calibration offset, and on the other edge where there is no radiation effect. SEM images of these imprints (Figure 8D) were acquired to increase the accuracy of projected contact areas. TriboScan on TriboIndenter over a 5 μm *5 μm small area (Figure 8A) was also used to validate the area measured by SEM (Figure 8B).

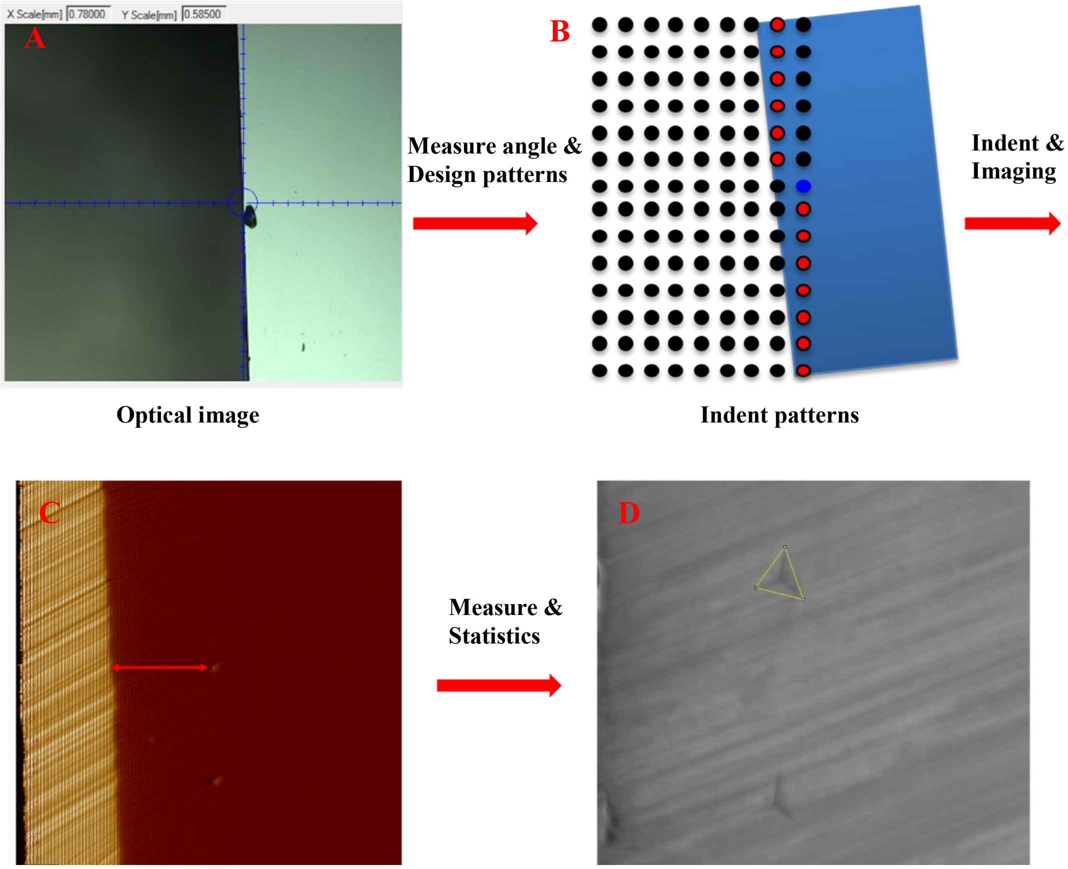

Optical image

Indent patterns

Figure 8 *Ex situ* nanoindentation test setup

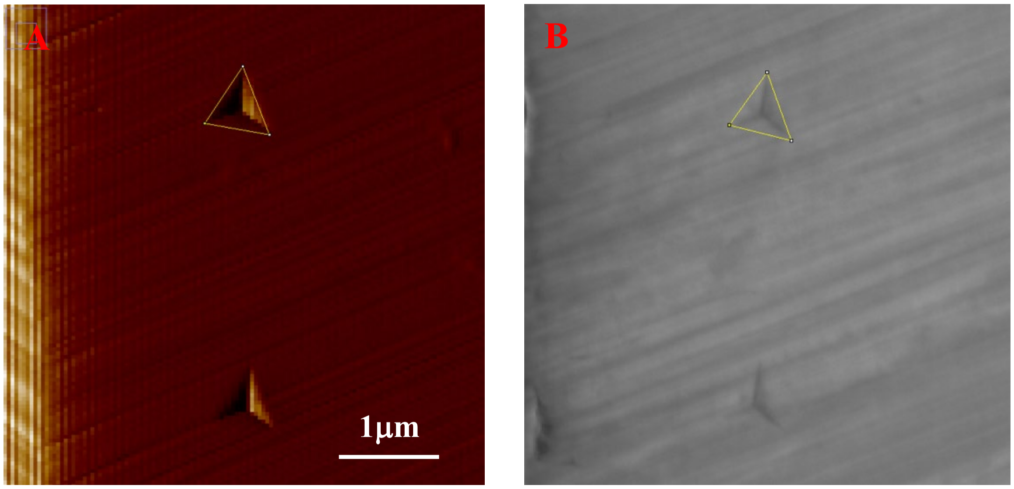

Figure 9 TriboScan image and SEM image of the same imprint to measure projected contact area. Yellow triangles are defined in ImageJ and both images have the same scale bar

Chapter 4 As-synthesized thin 3C-SiC mechanical properties

SiC is brittle in macroscopic studies but it can be become ductile when deformation occurs at smaller length scales (either small deformation volume or a small sample) and new phenomena have been reported at this scale. In this study, another deformation-related phenomenon that emerges in SiC at these scales have been observed. Previous studies of single crystal α-SiC polytypes (hexagonal) [87][88] and β-SiC (cubic) nanowires [89][90] have revealed unusual behaviors, such as phase transformations amongst different crystal polytypes, amorphization, and even super plasticity at room temperature, and these phenomena can occur during nanoindentation at different sample sizes and geometries. Here, we report direct observation of mechanical response and the underlying deformation mechanisms in thin polycrystalline 3C-SiC using *in situ* TEM nanoindentation tests. Our tests use a thin section geometry indented with a sharp tip, unlike previous pillar compression studies [88][87], and demonstrate plastic deformation arising from generation of dislocations and plastic deformation recovery during unloading. We speculate that these unusual behaviors emerge at certain nanoscale, especially sample thickness, and suggest that they may be useful validating models of nano or microscale deformation of 3C-SiC relevant to applications in MEMS/NEMS and thin coatings.

4.1 Sample thickness determination

Thickness measurement of thin samples is always challenging, but based on different sample performance we observed, thickness determination is quite important for this study. Here, I used energy filtered TEM to measure inelastic mean free path of 3C-SiC under specific microscope condition and therefore used the same mechanism of thickness measurement via electron energy loss spectroscopy (EELS) to determine sample thickness[91]. The equation is as follows:

$$t = \lambda \times \ln(\frac{I_t}{I_0}) \qquad (1)$$

t is the sample thickness, λ is inelastic mean free path, I_t is total intensity in the low-loss spectrum, and I_0 is the intensity of zero-loss peak.

A standard TEM sample of as-synthesized 3C-SiC was milled to an extreme wedge shape with thickness ranging from 80 nm to 400 nm. K2 camera was used to capture TEM images without any slit (Figure 10A) and with a 10 eV energy filter inserted (Figure 10B). Image software Digital Micrograph was used to generate a map of $\frac{I_t}{I_0}$, shown in Figure 11, by dividing the intensities in Figure 10. Therefore, with the three markers, the intensity can be coupled with a particular location respect to the markers. From Equation (1), inelastic mean free path λ is the slope of the linear equation. The thickness measurement of 16 different locations (Figure 12 shows 4 cuts with thicknesses of 8 positions) on the standard TEM sample was done in SEM and the curve fitting to get slope λ is as Figure 13. Thus, λ is 154 ± 2 nm. The thicknesses of all samples were measured under the same condition based on the λ value.

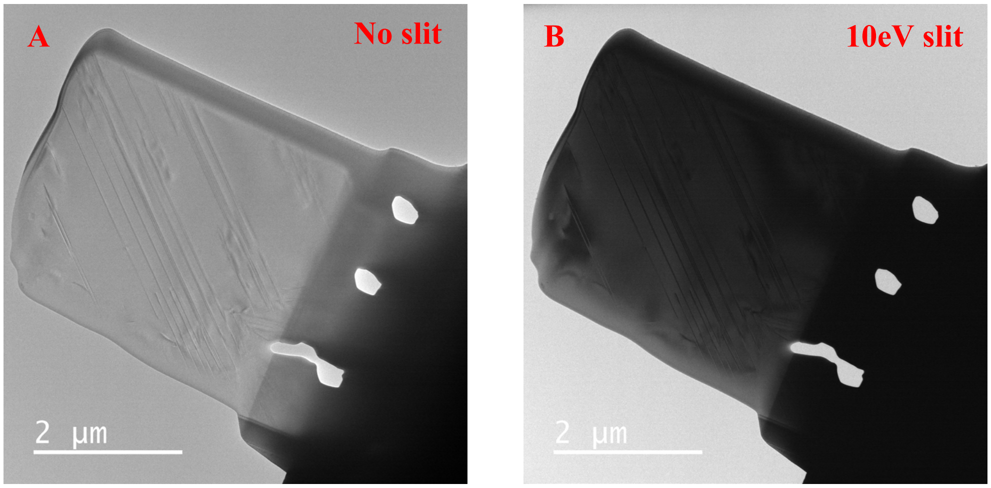

Figure 10 TEM images of 3C-SiC sample without and with energy filter

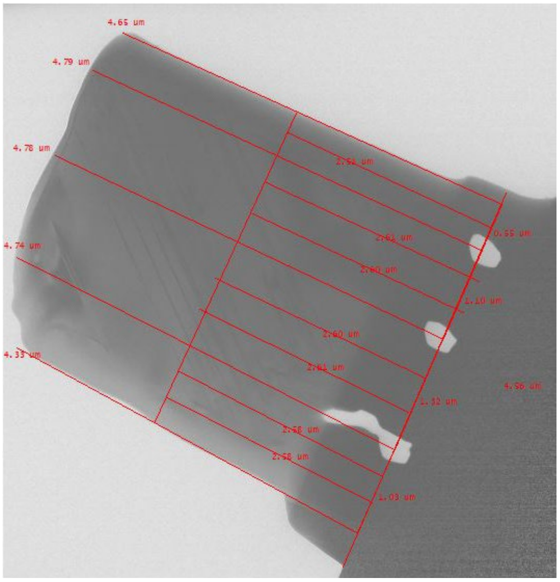

Figure 11 Analyzed image using Digital Micrograph with a map of intensity ratios

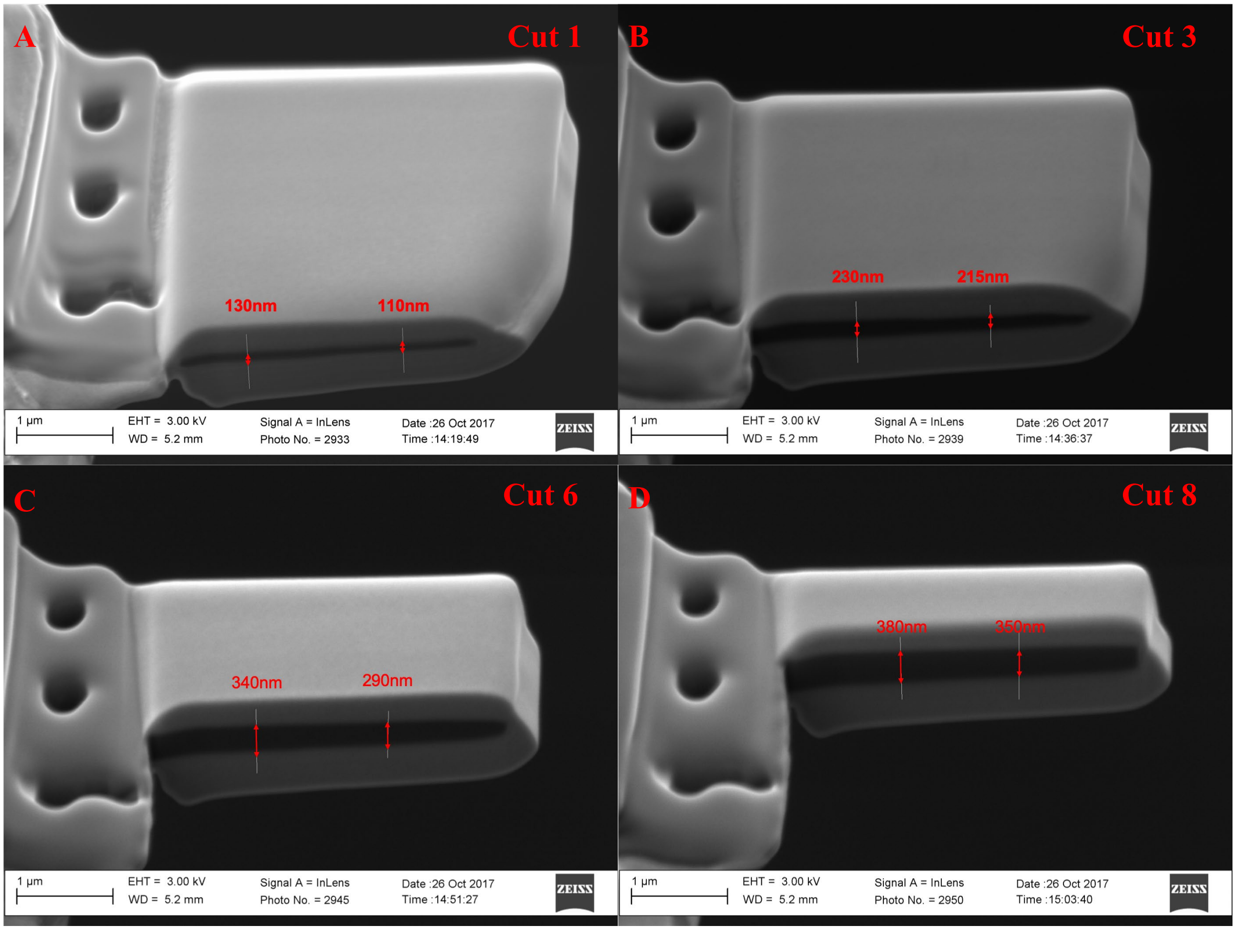

Figure 12 SEM images of 4 cuts with thickness measurement of 8 positions

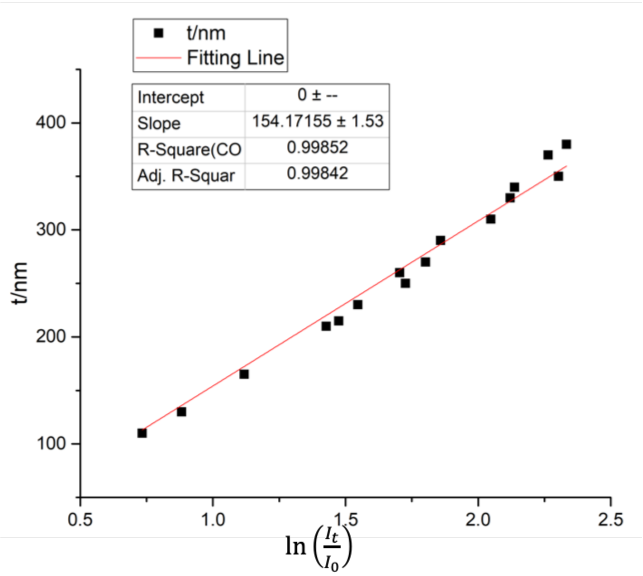

Intercept	0 ± --
Slope	154.17155 ± 1.53
R-Square(CO	0.99852
Adj. R-Squar	0.99842

Figure 13 Data fitting of Ln (I_t/I_0)-t curve to get inelastic mean free path

4.2 Fracture of thin 3C-SiC

3C-SiC is generally considered hard and brittle, so failure by fracture is expected based on macroscale experiments. Figure 14 shows an *in situ* indentation test with repeated stress drops and ultimate failure due to fracture. Figure 14B is the starting point of the test with the indenter just making contact with the sample and the force increasing. A drop of the force and a gap of the measured indenter displacement appear near 300 nm displacement (Figure 14A), and the TEM image in Figure 14C shows a corresponding small crack (a zoomed-in image near the crack is at the upper right corner). The second load / displacement jump in Figure 14A is corresponding to another crack shown in Figure 14D. Unloading brings the force quickly to zero, and after the indenter is completely removed, a large chunk of the sample is missing due to fracture, as shown in Figure 14E. The TEM sample in Figure 14 was about 80 nm thick. The same pattern of multiple short cracks with associated load / displacement jumps was observed for multiple indents, spread across 6 TEM samples with similar thickness (≤90 nm), demonstrating that this behavior is typical for *in situ* indentation testing on samples with near this thickness.

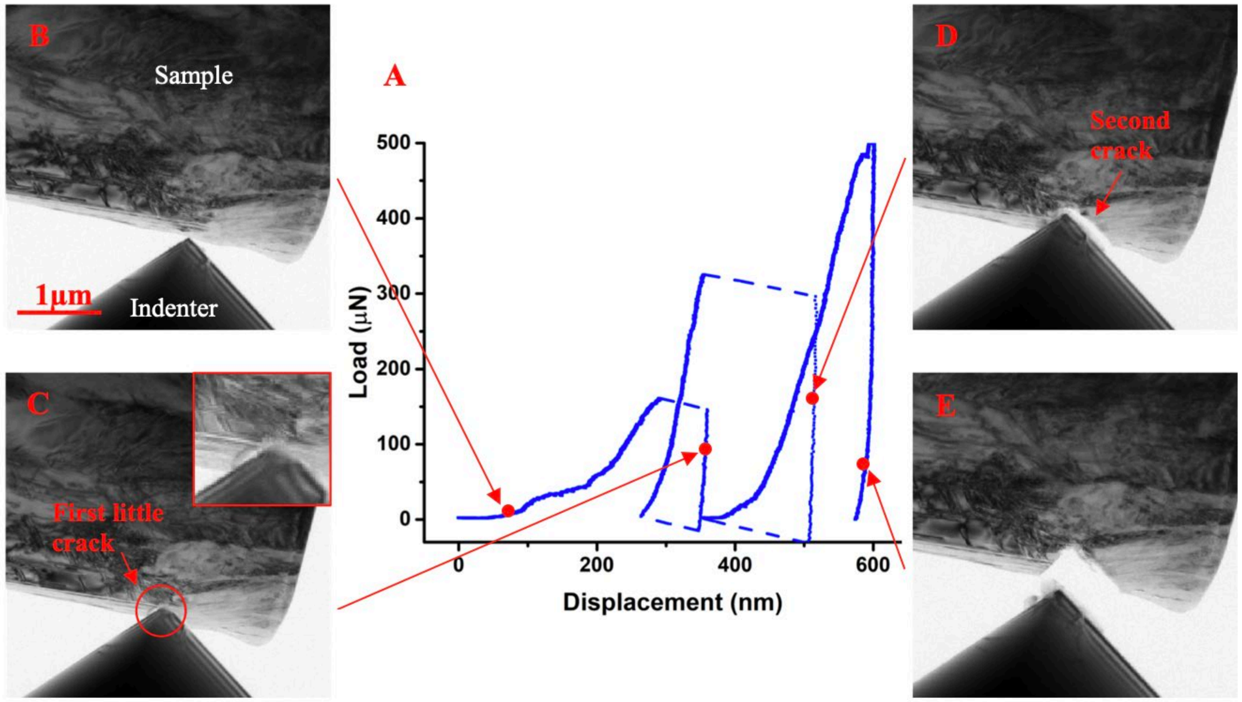

Figure 14 *In situ* indentation test exhibiting failure by cracking. A is the load-displacement curve measured from the holder transducer. B-E are bright-field TEM images captured from the video acquired during the test at the points indicated in A. C and D show small cracks. All the TEM images share the scale bar in B.

4.3 Brittle to ductile transition in thin 3C-SiC

Figure 15 shows an example of a test on a sample with thickness ~130 nm exhibiting quite different behavior. Figure 15A is the load-displacement curve data from the transducer and Figure 15B-F are bright-field TEM images from the video. The load-displacement curve is continuous without the gaps and force drops associated with cracking, and the images also show no evidence of cracking. Instead, during loading (Figure 15B-D), dark contours move consecutively away from the surface. These contours are bend contours arising from changes in the orientation of the diffracting crystal planes with respect to the beam direction [91][83]. This assignment was confirmed by tilting the sample after the test is complete and observing that most of the contours translate across the sample, as expected for bend contours. Similar contours have been observed in other *in situ* TEM compression tests on metals [92], silicon [93] and nanoparticles [94], and they can be used to visualize the evolution of the elastic strain field inside the samples [80][95][96].

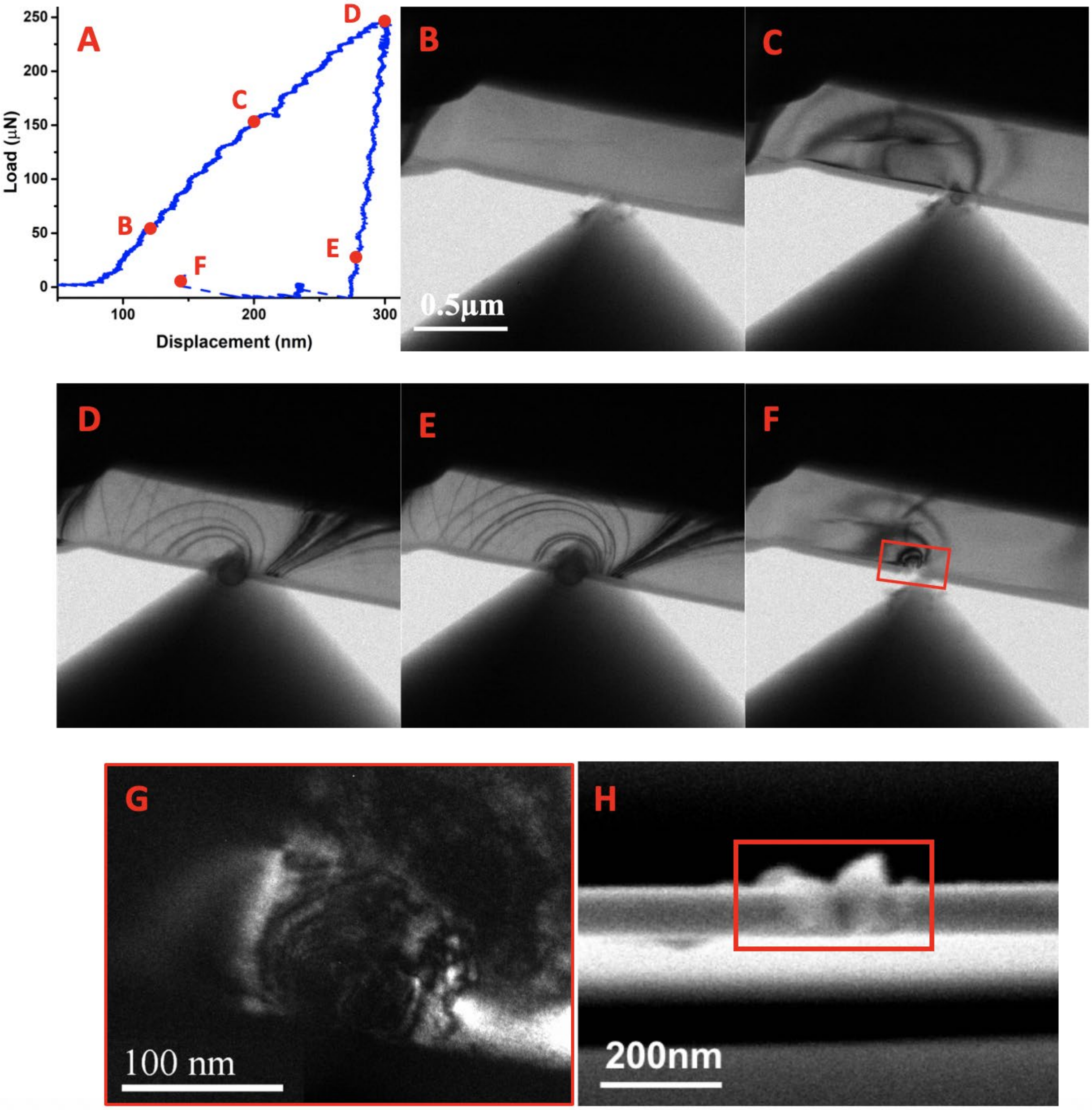

Figure 15 *In situ* indentation test showing room-temperature plastic deformation. A is the load-displacement curve and B-F are bright-field TEM images acquired during indentation. F is the TEM image after the indenter is removed from the sample. B-F share the same scale bar as is in B. G is a higher magnification dark-field TEM image of the position in the red frame in F. H is an SEM image of the imprint, viewed from the side, showing metal-like extrusion.

Upon unloading (Figure 15D-F), the contours retrace their paths toward the surface, but they do not completely disappear. Even when the indenter is fully retracted (Figure 15F), some bend contours remain, surrounding an imprint which is much smaller than the fractured area in Figure 14E. Figure 15H is the SEM image of the sample after indentation, viewing the sample in the direction from which the indenter came. There is a metal-like extrusion around the imprint due to the compression, which demonstrates plastic deformation of the sample during testing. The extrusion can be also seen from the TEM image after the indenter was removed, in Figure 2F. Figure 2G shows a higher magnification view of the part of the sample in the red square in Figure 2F, imaged with a $\langle 213 \rangle$ as the nearest zone axis with a $\{331\}$ reflection selected with the displaced aperture. The lines in the image are dislocations, which is confirmed because they do not translate across the sample when the sample is tilted, like the bend contours mentioned above. The creation of dislocations in the small area close to the imprint provides further evidence for residual plastic deformation. The residual strain from the plastic deformation prevents the bend contours near the imprint from disappearing completely. The shape and distribution of contours track the elastic strain, and they are similar to the strain fields in the extending cavity model [85], which describes deformation-affected areas in nanoindentation.

Figures 14 and 15 above illustrate that samples with different thicknesses exhibit qualitatively different behavior *in situ* under applied force in TEM, regardless of the starting microstructure. In Figure 16 we show accumulative probability of samples that exhibited plastic behavior with thickness smaller than the x-axis in our study. Analysis from indentation of more than 22 total samples, suggests a trend where samples with thickness smaller than 90 nm exhibit primarily brittle behavior with failure through cracking, as in Figure 14. Samples with thickness around 100 nm but no more than 270 nm exhibit some plastic deformation in addition to elastic deformation shown in Figure 15 and are less likely to fail by fracture in our tests. For really thin samples, linear elastic fracture mechanism does not apply, and critical stress intensity factor increase as thickness increases [97]. One hypothesis is that elastic field around the crack cannot relax stress enough to prevent fracture from happening, so its behavior is dominated by how many bonds that need to break. Another hypothesis is that plastic zone cannot be larger than the sample thickness, so that super thin samples have really limited plastic zone to relax stress, and fracture happens. Therefore, in this range thinner samples have lower toughness and are easier to fracture than thicker ones. However, samples with relatively larger thickness will exhibit some plasticity with mechanism discussed as below.

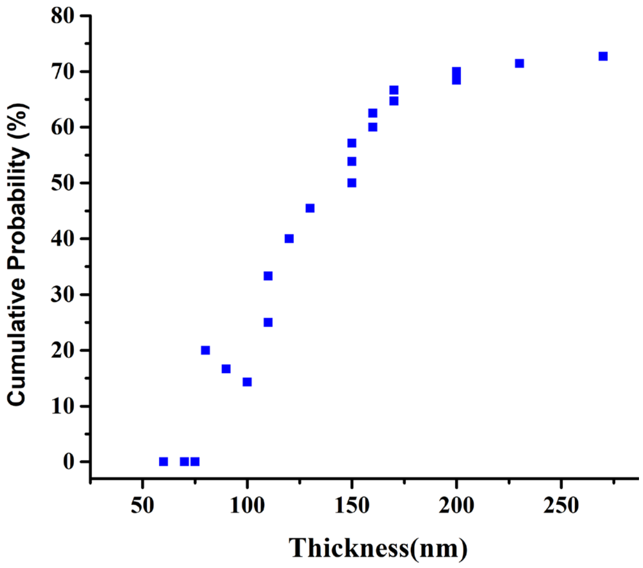

Figure 16 Accumulative probability of plastic deformation during indentation on 22 samples with thickness smaller than the x-axis thickness

Room-temperature plasticity in ceramic materials is not common, but it has been reported previously, for example in single crystal silicon [98] and strontium titanate [99]. Ceramics are more often ductile at high temperature, and Si and $SrTiO_3$ results show that decreasing sample size can reduce the brittle-to-ductile transition temperature to relatively low temperature. Molecular dynamics simulations predicted that single crystal silicon can plastically deform at room temperature by dislocations initiated from the surface [100]. In SiC, room temperature plasticity has been reported for different polytypes, but the explanation for the phenomena varies. In *in situ* SEM tensilte tests, Zhang *et al*. [89] observed single crystal 3C-SiC super plasticity at room temperature derived from dislocation activity induced amorphization, and Szlufarska *et al.* showed in simulations that amorphization of 3C-SiC is driven by coalescence of dislocation loops [101]. The same mechanism for plasticity was observed in *in situ* TEM compression tests of SiC nanowire by Han *et al*. [102]. Wang et al. [90] showed that plasticity in 3C-SiC nanowires arose from stretching, breaking and reforming of Si–C bonds in an intergranular amorphous film. A phase transformation from 4H to 3C of SiC under stress of 9 GPa was used to explain plasticity of 4H-SiC by Chen *et al*. [87], and compression tests on 6H-SiC nanopillars indicated that plasticity was controlled by glide of existing dislocations instead of newly generated ones, according to *Kiani et al*. [88].

Diffraction patterns acquired before and after indentation are indistinguishable (Figure 17), with no evidence of either amorphization or of a different phase. Therefore, phase transformation and amorphization are inconsistent with our experiments. The lack of phase transformation is not surprising, given the fact that pure 3C-SiC has to be annealed for several hours to transform to 6H-SiC [103], and 4H to 3C phase transformation can happen under 9GPa stress during 4H-SiC nano-pillar indentation to make 4H-SiC exhibit plasticity [87]. We therefore suggest that the observed plasticity must be mediated by the generation and propagation of dislocations. This is consistent with the metal-like surface extrusion surrounding the imprint, and we do directly observe dislocations in our TEM results after indentation (Fig.15 G). However, we do not directly observe creation and movement of dislocations in the movies acquired during indentation. We attribute this feature to the fact that dislocations in 3C-SiC created by *in situ* nanoindentation can only exist in a small region with low mobility and the diffraction condition could be unfavorable in this case to make dislocations visible.

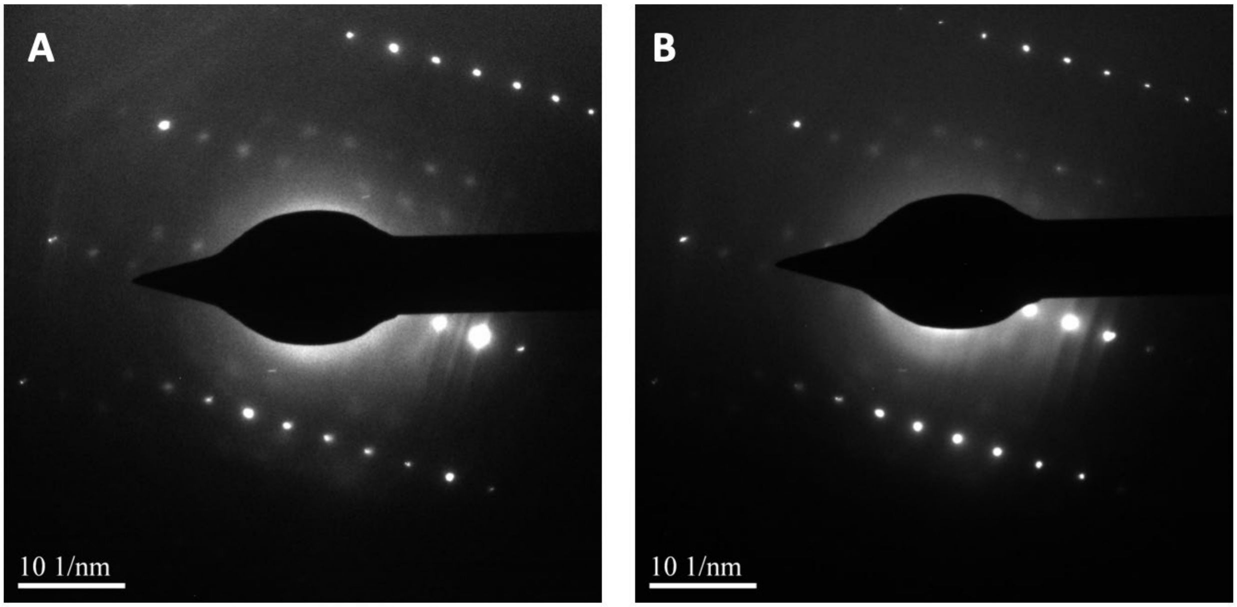

Figure 17 Diffraction patterns of area surrounding imprint before and after indentation test in Figure 2. A is before indentation and B is after indentation. The undistinguishable diffraction patterns demonstrate that there is no amorphization or phase transformation.

Due to the non-ideal indentation geometry and the difficulty of measuring the contact areas during *in situ* nanoindentation, accurate hardness and elastic modulus are difficult to obtain from the *in situ* load-displacement curves. We have estimated those quantities from a set of tests like shown in Figure 15, using standard nanoindentation formulae [85] without correction for the free-standing foil geometry, but with the real projected contact area measured from SEM images acquired after *in situ* testing (see Figure 15H). Based on load-displacement curves from *in situ* nanoindentation tests, we estimated the hardness to be 31 ± 2 GPa and modulus 180 ± 50 GPa. The hardness is in a reasonable agreement with 31 - 45 GPa from Ref [17][104], but the modulus is much lower than 350 - 450 GPa in Ref [105][13]. We performed *ex situ* indentation on these same samples (data not shown), which yielded hardness of 33 ± 3 GPa, and modulus of 320 ± 10 GPa, is consistent to the lower limit of the ranges of hardness and modulus in literature. Therefore, we ascribe the low value of the modulus in the *in situ* results to uncorrected size and edge effects. Quantitative analysis of *in situ* nanoindentation load-displacement data remains a challenge.

4.4 Plastic deformation recovery

Figure 18 shows an example of *in situ* nanoindentation test exhibiting plastic deformation recovery during unloading in a sample with thickness ~150 nm. Among 16 samples that had plastic deformation, more than 63% exhibited some plastic strain recovery, the rest did not recovery and failed during unloading. Features in the load-displacement curves used to identify plastic strain recovery are explained below. The load-displacement curve in Figure 18A shows that there is no fracture up to the same maximum displacement as in the data in Figures 14. Figures 18B-D show images acquired during loading and show the same kind of bend contours due to elastic and plastic deformation as shown in Figure 15. Figure 18I is an image of the sample after indentation, acquired with a <110> as the nearest zone axis with a {111} reflection selected with the displaced aperture, and it shows the plastically deformed area next to the imprint. The beginning of unloading corresponds to the image shown in Figure 18D, and, judging by the load-displacement curve, elastic deformation recovery is complete by Figure 18E. At that point, some of the bend contours have disappeared, but not all of them. As the indenter continues to retract, as shown in Figures 18E-H, bend contours keep moving backward toward the surface, and simultaneously the force periodically spikes above zero. The combination of continued micro-strain evolution and positive spikes in force (which indicate the sample pushing back on the indenter) suggest ongoing recovery of plastic strain during unloading. The residual plastic deformation after the full retraction of the indenter in Figure 18I shows that the recovery is not complete. The positive spikes in force from zero baseline (Figures 18E-G) after an elastic unloading (Figures 18D-E) can be explained by continued reverse movement of bend contours, which is a direct evidence of partial plastic strain recovery. In addition, the tail in the load-displacement curve in Figure 18A between points E and G is similar to the tail shown in stress-strain curve of nanocrystalline Al in large scale molecular dynamic simulations of plastic deformation recovery [106].

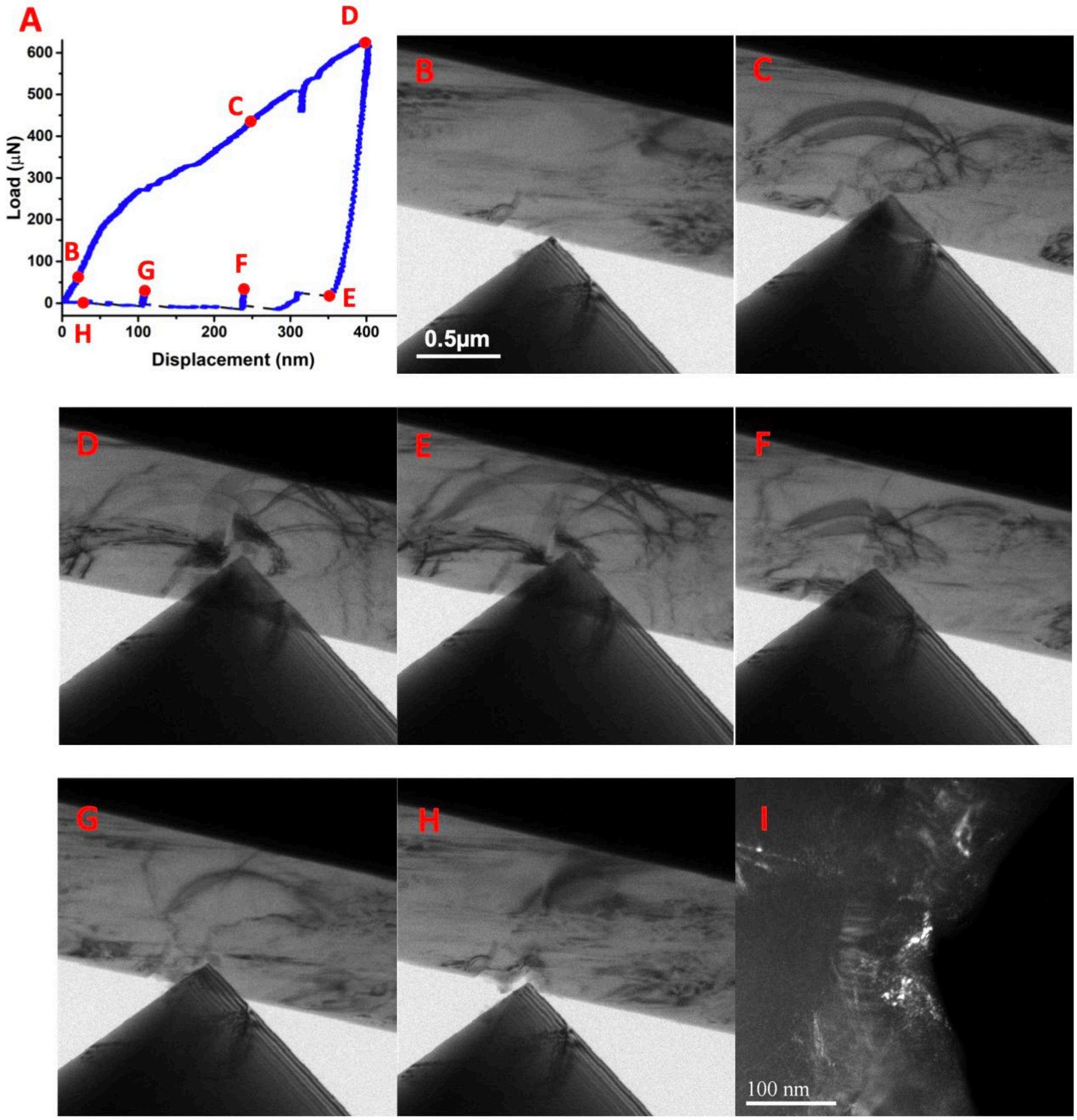

Figure 18 *In situ* nanoindentation test exhibiting plastic deformation recovery. A is the load-displacement curve during indentation, and B-H are bright-field TEM images acquired during indentation. B-D are during loading, and E-H are during unloading. B-H all have the same scale bar as is in B. I is the post-indentation dark-field TEM image of the indent after removing the indenter showing the region of defects associated with residual plastic deformation.

This kind of plastic strain recovery is rarely reported in *ex situ* indentation tests because without microstructural data collected during unloading, plastic strain recovery is difficult to detect. Plastic strain recovery has been reported by, for example, Rajagopalan *et al*. [107], but only in metals or alloys and the mechanisms varied from one study to another. These mechanisms include either one or a combination of the following: difference of grain size [108], inhomogeneities in the microstructure [107][108], reorganization of interface structures [109][110], dislocation annihilation [106], and grain boundary diffusion [111]. This range of mechanisms reported in literature suggests that the details of plastic strain recovery are strongly dependent on the specific microstructure of the samples. In our *in situ* TEM nanoindentation, dislocation lines could be extended by external force but did not reach the point where they became unstable and propagate spontaneously [112]. In addition, due to the small area where dislocations were observed, they barely interacted with other microstructural features and consequently were unlikely to become pinned. Based on the discussion above, we speculate that the extension of dislocations was reversed once the external force was retracted, which leads to the recovery of some plastic strain.

If plastic deformation recovery is reduced or blocked, perhaps by pre-existing microstructural features in the sample which can pin or absorb dislocations, even though the dislocations only exist in small area close to the imprint as discussed above, the sample can fracture but does not have to during unloading. Figure 19 shows an *in situ* indentation test on a sample with thickness ~110 nm, imaged entirely using dark-field TEM with an example of this kind of behavior. These data were acquired with a ⟨214⟩ as the nearest zone axis with a {422} reflection selected with the displaced aperture. Dark-field TEM was used in an attempt to highlight the contrast from dislocations. As shown in Figure 19C, bend contours are generated and move until the indenter starts to retract from the sample. Then the bend contours start to move back to the surface, as in Figure 19D. However, fracture happens after that, and many cracks are observed when the indenter is completely removed from the sample. The crack paths are the same shape as the last shapes of the bend contours which were moving back toward the surface. Sharp, narrow bend contours indicate high local curvature in the sample, so it appears that the fracture starts in a region of high local stress. The final result is similar to sample (Figure 14) that fractures during loading, without *in situ* observation of the indentation procedure, it will be treated as pure fracture and the plasticity of it will be ignored.

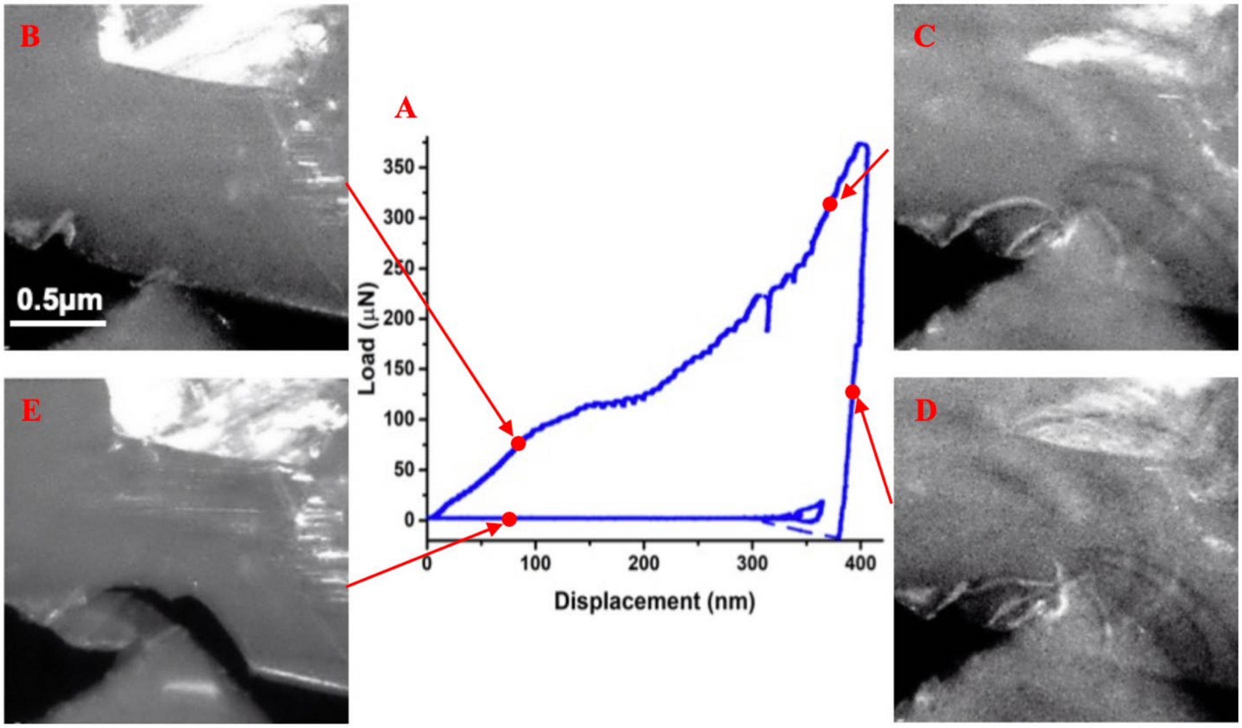

Figure 19 *In situ* nanoindentation test under dark-field TEM revealing fracture when plastic deformation recovery failed. A is the load-displacement curve, and B-E are dark-field TEM images acquired during indentation. B-E share the same scale bar as in B.

4.5 Conclusions

In situ nanoindentation tests on thin 3C-SiC in a transmission electron microscope show small but non-negligible plastic deformation at room temperature. SiC is brittle in macroscopic studies but it can be become ductile when deformation occurs at smaller length scales. We report brittle to ductile transition of 3C-SiC that emerges at these scales. During loading, bend contours arising from deformation move through the sample. After unloading, some contours remain, dislocations are created, and a metal-like extrusion surrounds the imprint, all indicating residual plastic deformation is derived from dislocation generation and propagation. The load-displacement curves and the backward movement of bend contours after indenter is retracted suggest some plastic deformation recovery after elastic deformation recovery during unloading. We suggest that plastic deformation recovery arises from annihilation of transient dislocation extension driven by retracted external stress. Both plastic deformation and plastic deformation recovery are likely related to certain nanoscale dimensions of the samples tested.

Chapter 5 Radiation effects on mechanical properties of thin 3C-SiC irradiated at different temperatures and fluences

5.1 Microstructure characterization of irradiated 3C-SiC in TEM

Before *in situ* nanoindentation tests, microstructural characterization of irradiated 3C-SiC samples was performed in TEM. Figure 20, Figure 21, and Figure 22 show the microstructures of SiC irradiated under 600 °C 0.3 dpa, 600 °C 3 dpa, and 900 °C 3 dpa. Labels indicate the direction of the incident carbon ions. Images with red frames are higher magnification views of the areas inside the red rectangles. All the samples share similar general microstructure. They are polycrystalline with several grains within the field of view, there are several pre-existing stacking faults, and a dark band caused by the end of range defects of the ions. The positions of the dark bands validate the SRIM simulation (Figure 3) showing that the peak of radiation damage is about 3.5 μm deep. The only difference amongst the sample is visible the radiation damage defects are at low magnification. In Figure 20A, areas of the 600 °C 0.3 dpa sample on either side of the dark band exhibit quite similar contrast. Only at higher magnification does the difference between radiated damaged area and non-irradiated area become obvious, as shown in Figure 20B. For the 600 °C 3 dpa and 900 °C 3 dpa samples, different contrast caused by radiation-induced defects can be distinguished at lower magnification (Figure 21A and Figure 22A), and at high magnification (Figure 21B and Figure 22B) radiation-induced defects are visible and there is a huge difference between irradiated areas and non-irradiated areas.

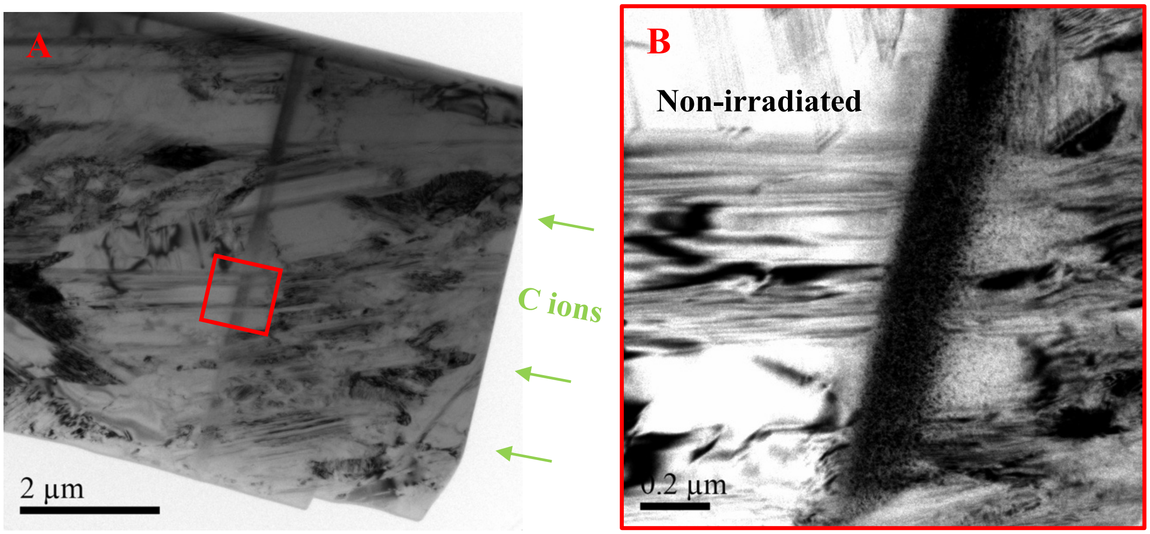

Figure 20 Bright field TEM images of 600 °C 0.3 dpa irradiated 3C-SiC with incident carbon ions from the right. A is at low magnification and B is the zoomed-in area of A.

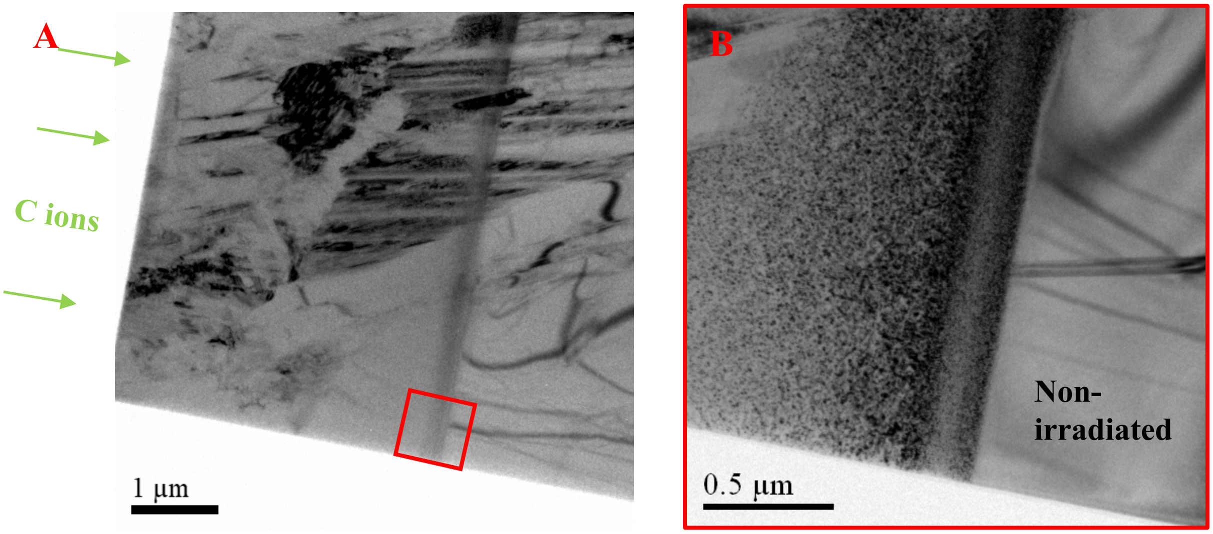

Figure 21 Bright field TEM images of 600 °C 3 dpa irradiated 3C-SiC with carbon ions incident from the left. A is low magnification and B is the zoomed-in area of A.

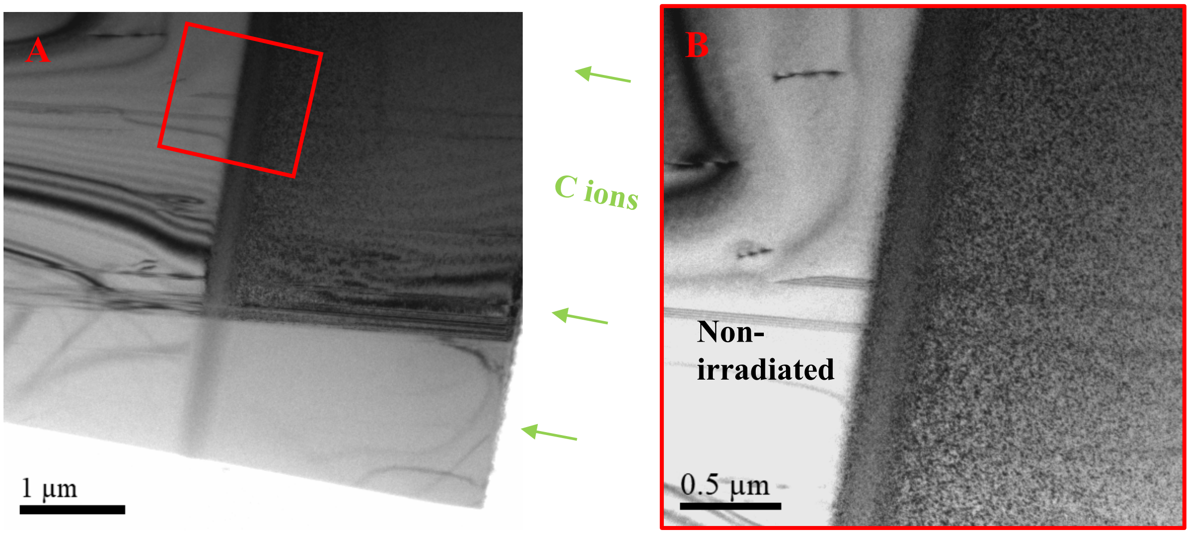

Figure 22 Bright field TEM images of 900 °C 3 dpa irradiated 3C-SiC with carbon ions incident from the right. A is at low magnification and B is the zoomed-in area of A.

Microstructure characterization on one sample along radiation damage depth was done as well on all three radiation conditions. Figure 23 is a standard TEM sample of 600 °C 0.3 dpa 3C-SiC with the radiation surface on top right and the centers of circles represent different observation positions (sizes of the circles do not proportional to real observation area, same color indicates same position but different magnifications). Figure 3 shows how radiation damage level along depth and for ion radiation, there is a huge change of radiation damage level towards the end of max radiation damage depth, and beyond that depth, there is no radiation damage. Based on the microstructure evolution discussion of 3C-SiC under different temperatures and different radiation fluences in Chapter 2, radiation-induced defects are expected to be BSDs and their clusters, and it is validated by the observation in TEM (Figure 23C-D) that there are no dislocation loops or networks, the only type of defect is point defect clusters. All images in Figure 23 were taken with <111> zone axis (DPs are inserted in the images at the corners). Red circle represents a non-irradiated area and there are only pre-existed stacking faults, no radiation-induced defects (Figure 23B). Radiation depth of blue area is about 1.5 μm and purple area is about 3 μm. Comparing Figure 23C and D, both the size and density of defects become much larger in Figure 23D, which is corresponding to the increase of damage level in Figure 3. Therefore, for the sample irradiated under 600 °C, when irradiation fluence increases from 0.3 dpa to about 4 dpa (estimation from SRIM simulation of certain radiation depth), radiation-induced defects type does not change, only defect size and density increase.

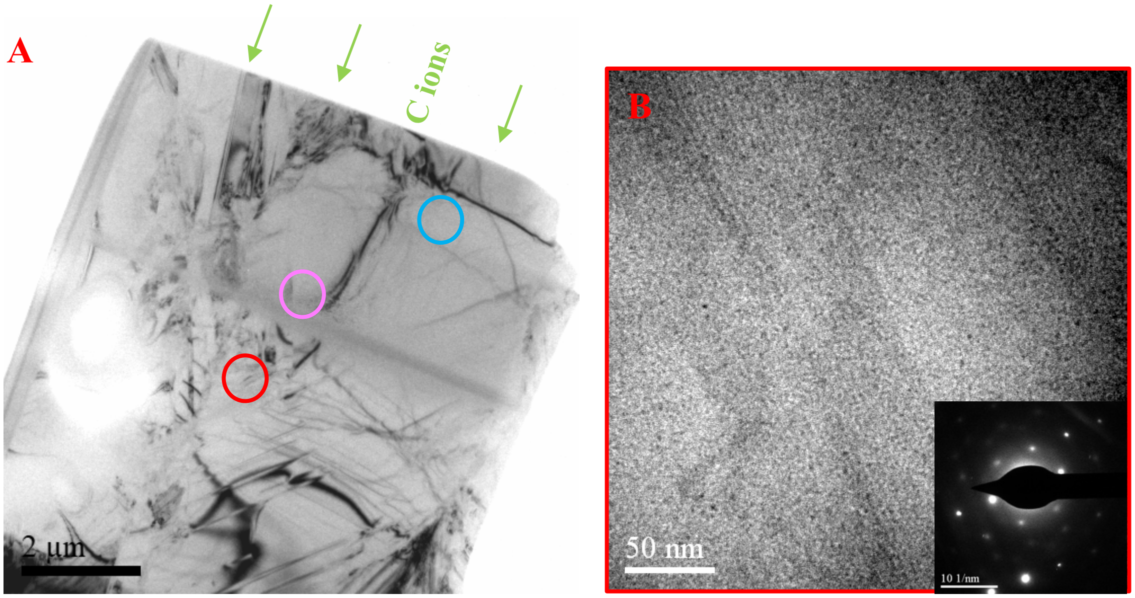

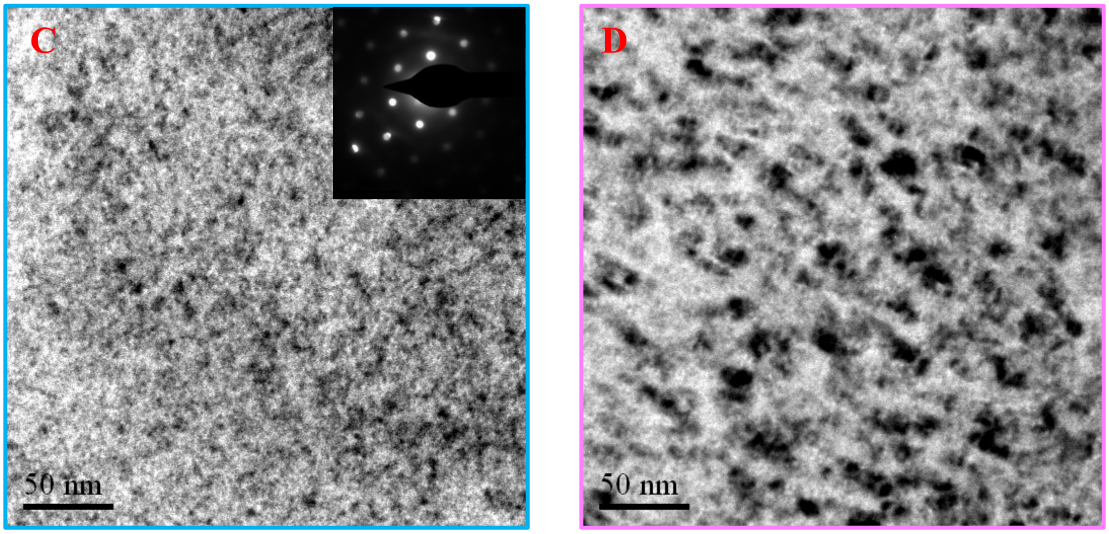

Figure 23 Microstructure characterization of 600 °C 3 dpa irradiated 3C-SiC along the irradiation depth. The sample is imaged along a <111> zone axis. A is a standard TEM sample at low magnification. The colors in A mark the positions of the images in the corresponding color frames. B is the image from a non-irradiated area. C is from an irradiated area with radiation depth 3 µm, and D is from radiation depth 1.5 µm.

5.2 *In situ* nanoindentation tests on 3C-SiC under different radiation conditions

5.2.1 *In situ* nanoindentation tests on 600 °C 0.3 dpa 3C-SiC

Figure 24 shows the performance of one sample with thickness about 100 nm under *in situ* nanoindentation test (Sample 5 in Table 2). Figure 24B-F are corresponding to the points labelled in Figure 24A. Due to the low radiation fluence and orientation of grains, the radiation-induced defects are not visible at times during indentation tests. But the max radiation damage depth band is visible most of the time, and for the sample in Figure 24, the left side of the band is where there is radiation damage. The indentation is performed around 2.3 µm away from radiation surface.

Some of the large fluctuations in Figure 24A during loading are experimental artifact due to the motion of indenter and the instability of the system. Figurer 24B shows that the indenter starts to touch the sample and there are a lot of contours generated and moving due to elastic deformation in C. While fracture happens right after C when the displacement is about 45 nm, and there is a crack that can be seen in D, and at the same time, the load drops to zero and there is a gap of load between C and D. By fracturing, the sample releases the concentrated stress in a sudden but there is still contact between indenter and sample, so the force goes back up again. When retracting the indenter, crack or any debris around crack touches the indenter again due to the movement of the indenter, that causes the complex fluctuation in A between E and F. A long, straight and single crack path with thickness ~470 nm remains in the sample (Figure 24F). The performance of non-irradiated area with the same thickness on the same sample is similar to as-synthesized 3C-SiC, which experiences elastic deformation and plastic deformation (Chapter 4). Figure 25 exhibits the comparison of imprints between the irradiated area and non-irradiated area of the sample. There is almost no imprint left on the irradiated area after indentation, while the non-irradiated area has an imprint left (Figure 25A and B). From the image observing from the top (a little side way) of the sample, in figure 25C, the "stair" shape represents the crack underneath; in figure 25D, the imprint can be seen as well. The behaviors of irradiated area and non-irradiated area on the same sample are different, and irradiated area is more brittle and fractures.

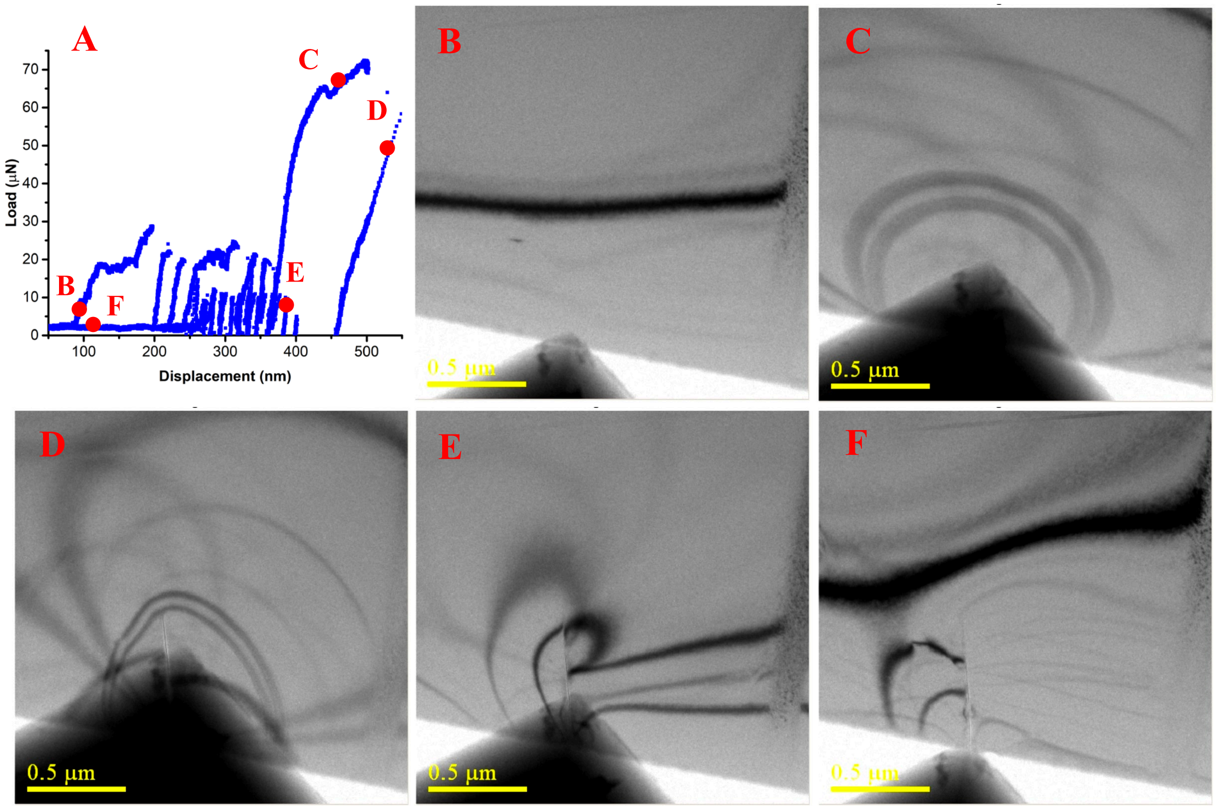

Figure 24 *In situ* nanoindentation test on 3C-SiC (Sample 5 in Table 2) irradiated under 600 °C 0.3 dpa. A is the load-displacement curve marked with corresponding moments for the images B-F. B-F are image sequences from the video of *in situ* nanoindentation test, B and C during loading and D-F during unloading.

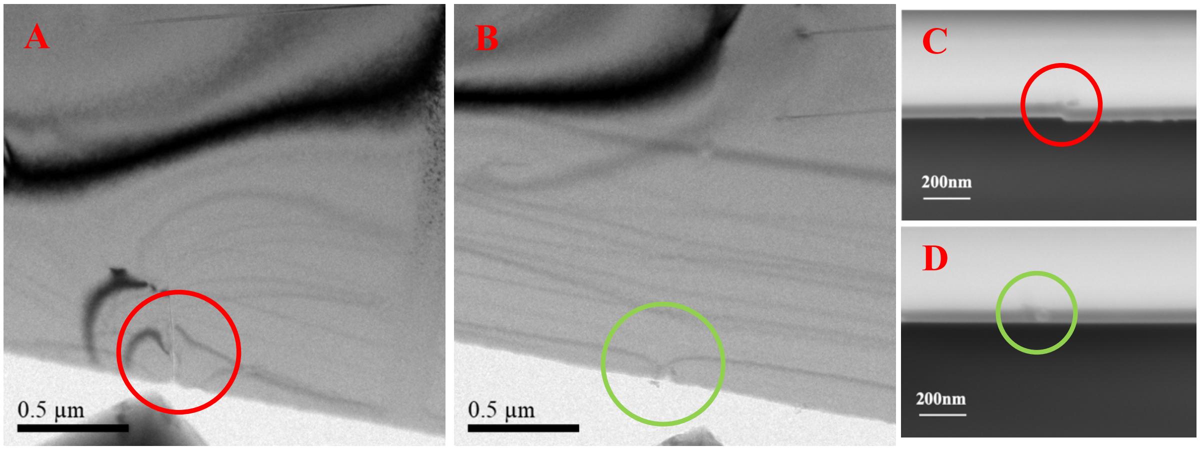

Figure 25 Comparison of the microstructure after *in situ* indentation between irradiated area A and non-irradiated area B in 600 °C 0.3 dpa 3C-SiC (Sample 5 in Table 2). C and D are SEM images from top view of A and B imprint after indentation test.

Figure 26 illustrates another kind of behavior that happens during *in situ* nanoindentation, and the sample is also irradiated under 600 °C 0.3 dpa with thickness ~200 nm. Indentation is performed in the irradiated area with radiation depth about 2 μm, and the defects are not quite visible due to the thickness of the sample and contrast tuned by other microstructures. As shown in Figure 26A, the force quickly reaches 125 μN, and drops to zero, which means that fracture happens. Figure 26B is during loading and C is after fracture. The fracture happens within one frame of the video. The post observation of the indentation is Figure 27A, in which there is no imprint and the crack paths are from two sides forming a semicircle. Moreover, the crack also happens in the direction parallel to the thickness of the sample, and half of the sample fractures. Same *in situ* nanoindentation is also done on the same sample but on the non-irradiate area and the there is an imprint left on top of the sample (Figure 27B) like the imprint left on as-synthesized sample.

In general. After irradiated under 600 °C 0.3 dpa, 3C-SiC loses its plasticity, becomes more brittle, and different failure behavior happens during nanoindentation tests. Table 2 is the summary of all results from reliable testing.

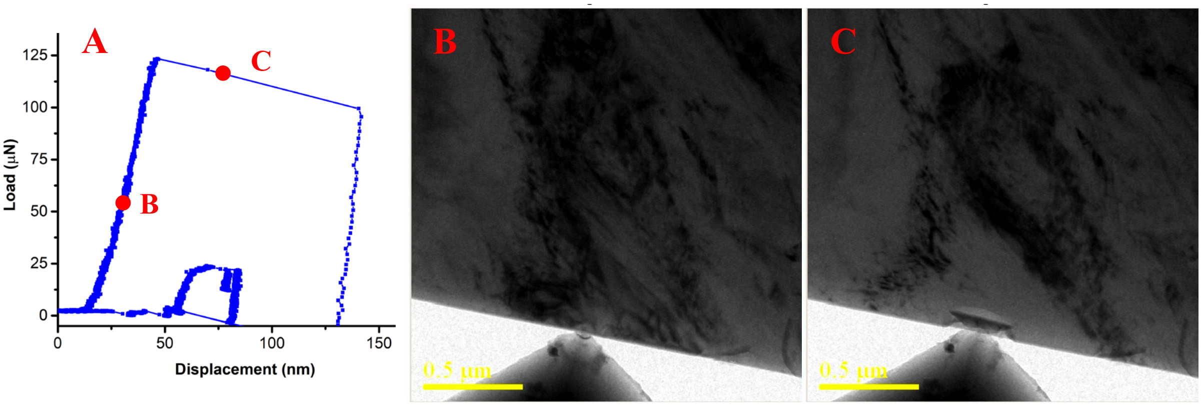

Figure 26 *In situ* nanoindentation test on 3C-SiC (Sample 7 in Table 2) irradiated under 600 °C 0.3 dpa. A is the load-displacement curve marked with corresponding moments of B and C. B-C are image sequences from the video of *in situ* nanoindentation test.

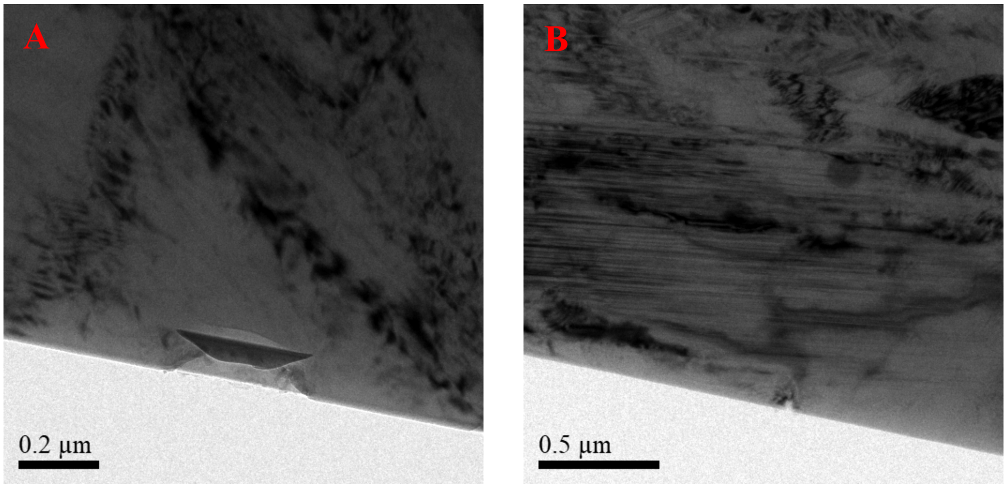

Figure 27 Comparison between irradiated area A and non-irradiated area B in 600 °C 0.3 dpa 3C-SiC (Sample 7 in Table 2) after *in situ* nanoindentation tests.

Table 2 Summary of *in situ* nanoindentation tests on 600 °C 0.3 dpa 3C-SiC samples with comparison to unirradiated area on the same sample. Fracture position represent where the cracks are with respect to the indentation positions. Crack shape and length describe fractography, in which simple and clear means few debris or microcracking. Fracture force for samples that fractured and max force for samples that did not fracture. Similar force means that stresses on both irradiated area and unirradiated area are similar, but the force can be influenced by indentation condition as well.

Sample #	Thickness (nm)	Radiated	Fracture	Fracture Position	Crack Shape	Crack length(nm)	Fracture force or max force (μN)
1	160	Y	Y	Two sides	Simple and clear	400	165
			Y	Two sides	Simple and clear	420	183
		N	Y	Two sides	Complex	300	300
			N	n/a	n/a	n/a	200
			N	n/a	n/a	n/a	470
5	100	Y	Y	Center	Simple and clear	470	73
		N	N	n/a	n/a	n/a	40
7	200	Y	Y	Two sides	Simple but not through the whole thickness	120	125
		N	N	n/a	n/a	n/a	150
10	250	Y	Y	Center	Simple but not through the whole thickness	170-500	180
		N	N	n/a	n/a	n/a	325

5.2.2 *In situ* nanoindentation tests on 600 °C 3 dpa 3C-SiC

To keep the radiation temperature the same 600 °C, while vary the radiation fluence, another set of samples were tested. Figure 28 indicates the performance of a 3C-SiC sample irradiated at 600C 3 dpa under nanoindentation tests, and A is the load-displacement curve. Sample thickness is around 90 nm and the indentation position is 2.4 μm away from radiation surface. Even though there are some force drops at B and C points, the images of those moments in Figure B and C do not exhibit any fracture, and the sample is experiencing elastic deformation with continued movement of contours. It is most likely to be artifacts when the indenter misses the sample a bit due to some vibration and quickly back to normal. With the *in situ* observation, those points on the load-displacement curve will be avoided being misunderstood to be some ‘pop-up’ events. Figure 28D is the moment right before a big gap appears in Figure 28A, and there is a huge crack shows up in Figure 28E and F is during unloading. The crack path propagated along the indenter tip straightforwardly. During the whole indentation, radiation-induced defects are visible in the area, however, there is no observation of any change of radiation defects under applied force, the ‘disappearance’ of defects in some area comes in Figure C-E is from the change of crystal orientation relative to the beam direction. Thus, there is no observable evolution of radiation defects or interaction between defects and applied stress during indentation test.

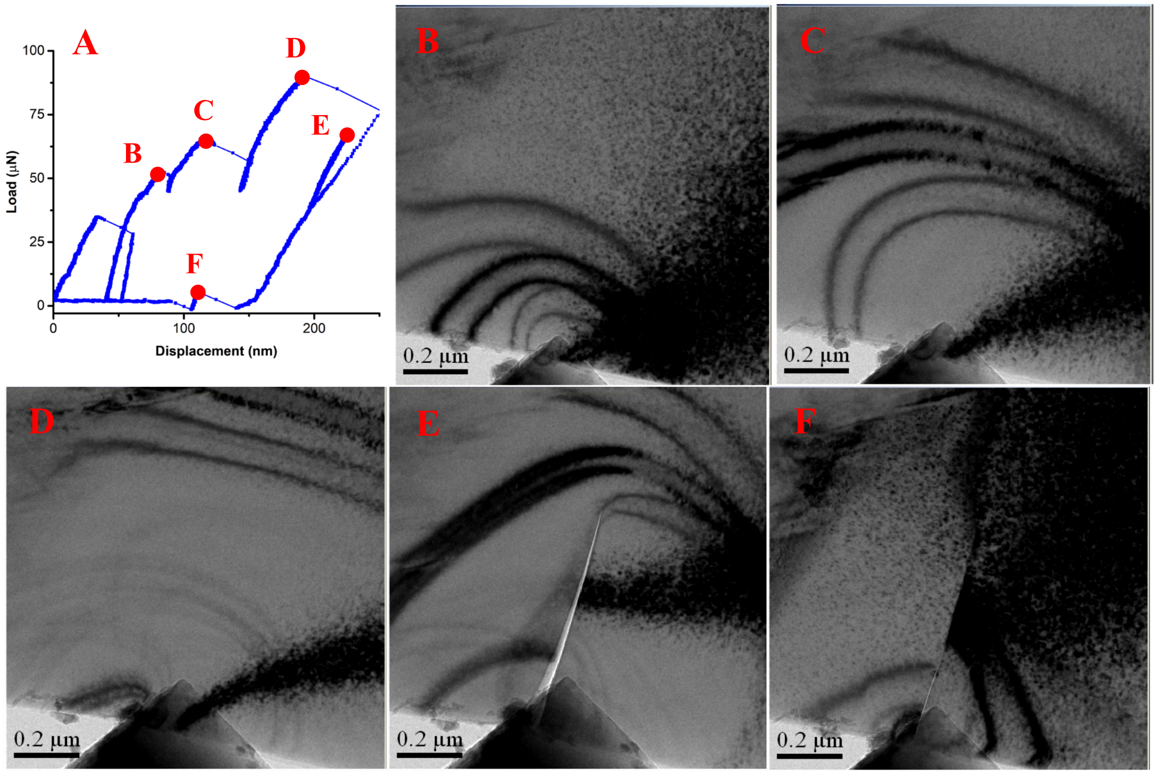

Figure 28 *In situ* nanoindentation test on 3C-SiC (Sample 1 in Table 3) irradiated under 600 °C 3 dpa. A is the load-displacement curve marked with corresponding moments of B-F. B-F are image sequences from the video of *in situ* nanoindentation test.

Similar *in situ* nanoindentation test has been done on the non-irradiated area on the same sample. The behavior is the same as as-synthesized 3C-SiC as expected and the post-indentation TEM image is in Figure 29 with the image of irradiated area mentioned above. Compared with the metal-like extrusion around small imprint left on non-irradiated area (Figure 29B), irradiated area fractures and there is only a straight and long crack left without any imprint on the surface (Figure 29A). The length of crack path is about 700 nm and there is no plastic deformation during indentation. Therefore, after irradiated at 600 °C 3 dpa, 3C-SiC is more brittle and fracture happens during indentation tests.

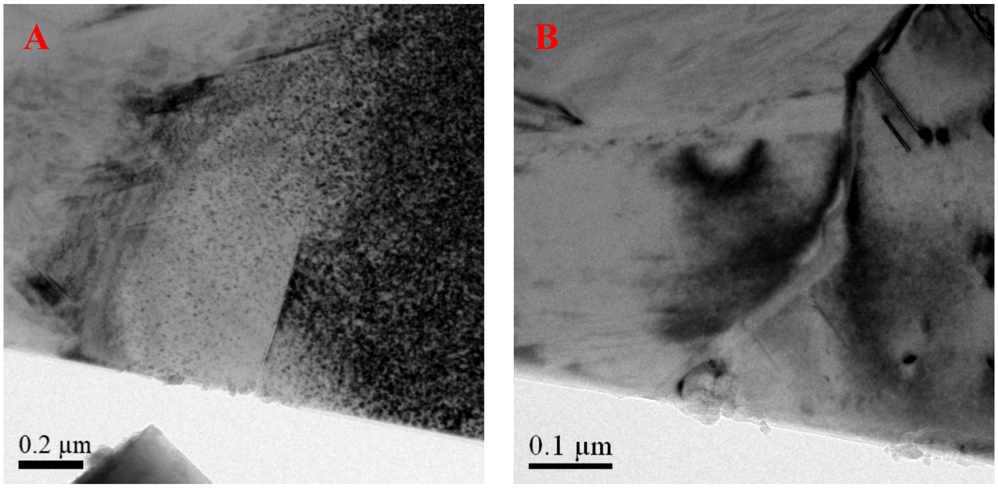

Figure 29 Comparison between irradiated area A and non-irradiated area B in 600 °C 3 dpa 3C-SiC (Sample 1 in Table 3) after *in situ* nanoindentation tests.

Under the same radiation condition 600 °C 3 dpa, another sample with thickness ~185 nm is under *in situ* nanoindentation test and its performance is shown in Figure 30. A is the load-displacement curve in which there is a force drop around D point. In B-D images, the sample has elastic deformation, contours are generated and moving in the sample until E moment, in which image the sample fractured instantly. After retracting the indenter, there is a long straight crack path in the center and the sample also fractures on both sides, as in Figure 30F. The sample fractures within the time of one frame, so which kind of crack formed first is unknown. The length of the straight crack is about 530 nm and fracture path from the sides are more complex than the sample shown in Figure 28. The summary other successful *in situ* nanoindentation tests on 3C-SiC irradiated at 600 °C 3 dpa is in Table 3. To sum up, samples in this group is more brittle than as-synthesized 3C-SiC, and fracture happens with longer straight crack path affecting larger areas than samples irradiated under 0.3 dpa. Detailed comparison will be in the discussion and conclusion section of this chapter.

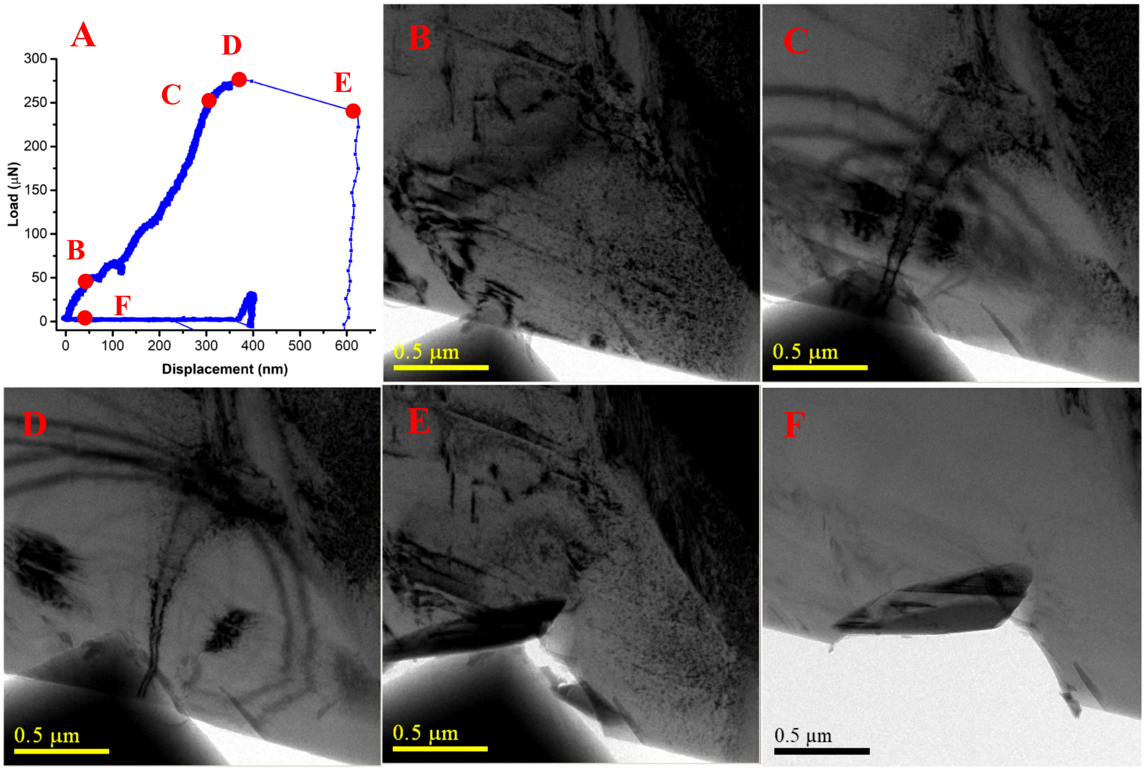

Figure 30 *In situ* nanoindentation test on 3C-SiC (Sample Thick 4 in Table 3) irradiated under 600 °C 3 dpa. A is the load-displacement curve marked with corresponding moments of B-F. B-F are image sequences from the video of *in situ* nanoindentation test.

Table 3 Summary of *in situ* nanoindentation tests on 600 °C 3 dpa 3C-SiC samples with comparison to unirradiated area on the same sample. Fracture position represent where the cracks are with respect to the indentation positions. Crack shape and length describe fractography, in which complex means some debris or microcracking. Fracture force for samples that fractured and max force for samples that did not fracture. Similar force means that stresses on both irradiated area and unirradiated area are similar, but the force can be influenced by indentation condition as well.

Sample #	Thickness (nm)	Radiated	Fracture	Fracture position	Crack Shape	Crack length (nm)	Fracture force or max force (μN)
1	90	Y	Y	Center	Simple and straight	700	90
		N	N	n/a	n/a	n/a	83
2	100	Y	Y	Center	Simple and straight	820	91
		N	Y	Center and sides	Complex	300	85
4	100	Y	Y	Center and sides	Simple and straight	810	115
		N	Y	Center and sides	Complex	400	82
6	70	Y	Y	Center and one side	Simple and straight	350	15
		N	N	n/a	n/a	n/a	26
Thick 2	160	Y	Y	Center	Simple and straight	780	163
		N	N	n/a	n/a	n/a	120
Thick 4	185	Y	Y	Center and sides	Straight but sides are complex	530	280
		N	N	n/a	n/a	n/a	310

5.2.3 *In situ* nanoindentation tests on 900 °C 3 dpa 3C-SiC

To keep the radiation fluence the same as 3 dpa, radiation temperature increases from 600 °C to 900 °C. This set of samples irradiated under 900 °C 3 dpa, with thickness ranging from 100 nm to 250 nm, perform under applied force in the way shown in Figure 31. A is the load-displacement curve and it is smooth without any drops or gaps, similar to Figure 15A and 18A, which means that based on the curve, there is no fracture or sample failure happens during indentation. From image sequences Figure 31B-F, the sample is behaving the same as as-synthesized 3C-SiC sample: generating contours during elastic deformation, then some plastic deformation followed by some plastic deformation recovery. To compare the imprints left on irradiated area (Figure 32A) and non-irradiated area (Figure 32B), SEM images from top view of the same sample were taken and are in Figure 32. Both A and B images have the characteristic extrusion around the imprint indicating plastic flow and there is no noticeable difference.

Four more samples with 7 more indentation tests on the irradiated area have been performed, and only one relatively thin sample fractures. Most of the indentation results are similar to as-synthesized 3C-SiC even though the samples are irradiated. Based on the *in situ* nanoindentation results, samples irradiated under 900 °C 3 dpa are less brittle and deforms plastically during indentation tests.

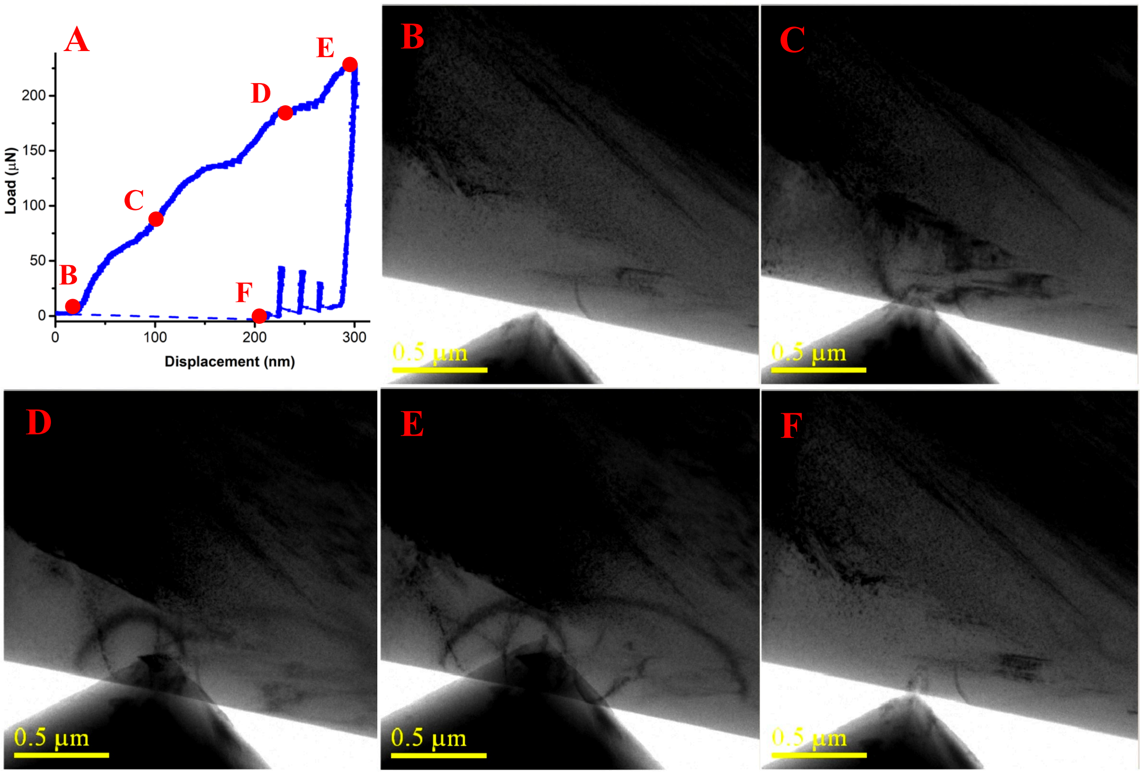

Figure 31 *In situ* nanoindentation test on 3C-SiC irradiated under 900 °C 3 dpa. A is the load-displacement curve marked with corresponding moments of B-F. B-F are image sequences from the video of *in situ* nanoindentation test.

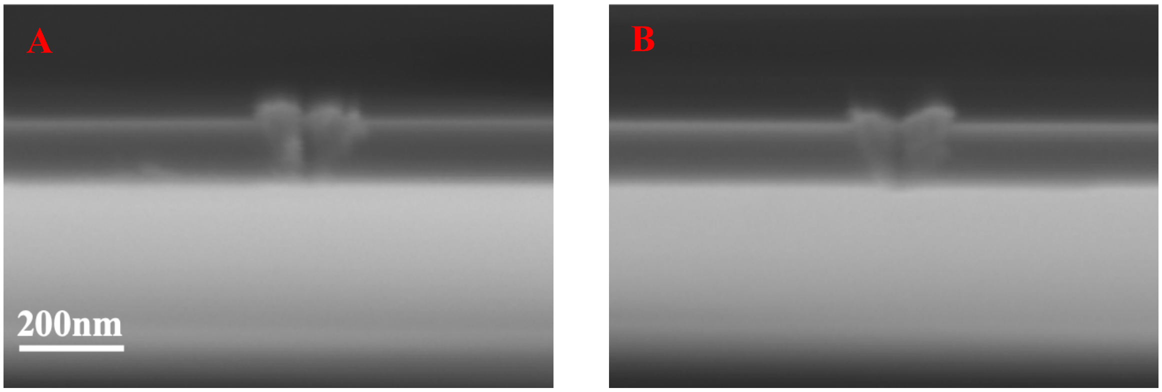

Figure 32 Comparison of imprint on irradiated area A and non-irradiated area B in 900 °C 3 dpa 3C-SiC after *in situ* nanoindentation tests observed from top.

5.3 Discussion and conclusion

Table 4 summarizes the characteristics of all of the *in situ* TEM nanoindentation tests. It compares the behavior of as-synthesized 3C-SiC and 3C-SiC irradiated under different radiation conditions, showing, for example, how likely the sample is to fail, and crack lengths and shapes. Table 4 only include results of irradiated samples within the thickness range for which unirrated samples are likely to plastically deform (80 nm – 250 nm). 67% of samples irradiated at 600 °C 0.3 dpa fractured, in which 60% of indentation results in the side cracking like Figure 26, and 40% of indentation results in the short, straight and simple cernter cracking like Figure 24. At a fluence of 3 dpa, samples irradiate at the same 600 °C are more likely to fracture and a long, straight and simple crack path was left after every test, as in Figure 29 and Figure 30. However, at 3 dpa and 900 °C, samples were more likely to deformed plastically again with small imprint left behind, similar to the as as-synthesized 3C-SiC samples. To summarize: Unirradiated samples deform plastically. Samples irradiated at 600 °C are tend to fracture, with longer, straighter cracks as the dpa increases. Samples irradiated at 900 °C deform plastically again. Due to the special small thickness of samples in this study, it is called resistance to cracking, to be distinguished from other close-related macroscale properties, such as toughness and fracture toughness.

Table 4 Summary of all irradiated 3C-SiC *in situ* nanoindentation tests including radiation conditions, probability of fracture, fractography, and probability of different fracture behaviors. The sizes of features and sample are not proportional the real size in the fracture schematic column.

Sample condition	Fracture percentage (fractured / total tests)	Crack path	Crack length/nm	Fracture schematic	Probability of this kind of fracture
As synthesized	17% (3/18)	Barely fracture	n/a		100%
600 °C 0.3 dpa	67% (4/6)	Center or sides	350±100		60%
					40%
600 °C 3 dpa	86% (6/7)	Center or center with sides	700±150		50%
					50%
900 °C 3 dpa	20% (1/5)	Almost the same as unirradiated	n/a		100%

Table 5 Summary of sample property trend based on literature and this study. Change of swelling is based on Ref. [2] [47] [58] [60] [64] [65], trends of room-temperature conductivity and thermal

defect resistance are based on Ref. [2] [71] [72] and Ref. [71] [113] [114]. Resistance to cracking, defect type/concentration and fracture toughness are based on results from this study.

Samples	Swelling	RT thermal conductivity	Thermal defect resistance	Resistance to cracking	Defect types and/or concentration		Fracture toughness
600 °C 3 dpa	Increase ↑	↓ Increase	Increase ↑	↓ Increase	BSDs and Clusters	Increase ↑	↓ Increase
600 °C 0.3 dpa					BSDs and Clusters		
900 °C 3 dpa					Small loops		
As synthesized					n/a		

Other properties of 3C-SiC, including swelling and thermal conductivity, are influenced by radiation conditions can be in a similar way. Table 5 collects some of those properties and how they are influence by radiation based on results from this study and from the literature. Figure 33 shows microstructure characterization results on all three sets of irradiated 3C-SiC. To aid visual comparison, A, B and C, representing microstructure in 600 °C 0.3 dpa, 600 °C 3 dpa, and 900 °C 3 dpa irradiated 3C-SiC, respectively, all share the same scale bar. D is the zoomed-in image of the red rectangle area in C. Defects in both 600 °C 0.3 dpa sample (A) and 600 °C 3 dpa sample (B) are BSDs and their clusters, but defects in 900 °C 3 dpa (C and D) are mostly small loops. The loop character is easier to see in Figure 33D. Furthermore, 600 °C 3 dpa sample has the highest defect concentration. Table 5 summarizes defect properties as well.

Swelling is the sign that radiation has effects on SiC and it can be measured and observed on bulk material. Therefore, it is important to mechanical properties and a lot of radiation-induced change of other properties can be explained by defect-induced lattice expansion, which is the main mechanism of swelling in low temperature range [60]. At 600 °C and 900 °C radiation condition, swelling falls into the point-defect dominated regime, which is between 150 °C and 1000 °C [2]. The maximum swelling is as large as 2% [55][58][64]. Unrecovered interstitial point defects or/and their clusters lead to lattice expansion. Firstly, swelling decreases as temperature increases due to defect recovery and recombination [47], so swelling of 900°C samples are the smaller than 600 °C samples. Secondly, swelling is affected by radiation fluence, but there is a saturation fluence that depends on temperature [2]. The lattice expansion saturated after ~0.1 dpa neutron radiation between 380 °C and 1180 °C in Ref [64], and X-ray diffractometry measurement of lattice parameters of 3C-SiC neutron irradiated at ~500 °C 0.3 dpa and 2 dpa is in good agreement [65]. Therefore, we speculate that swelling of samples irradiated at 600 °C 0.3 dpa and 600 °C 3 dpa should be similar. However, due to the different sensitivity of swelling to radiation fluence and temperature from resistance to cracking, they don't share the exact same trend.

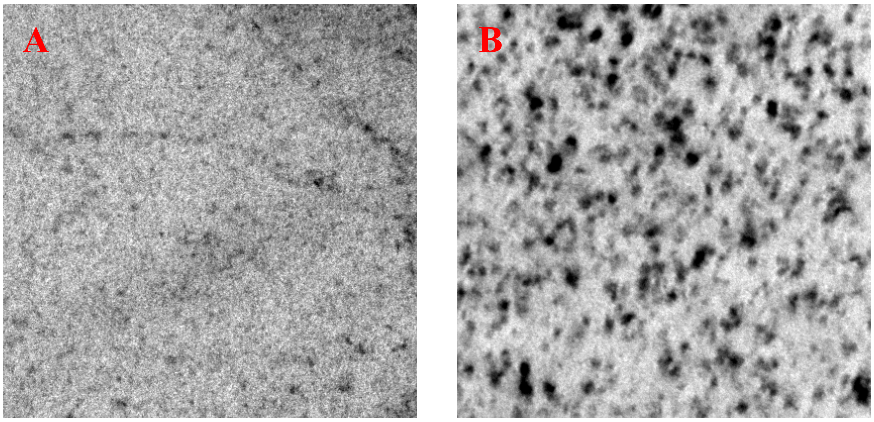

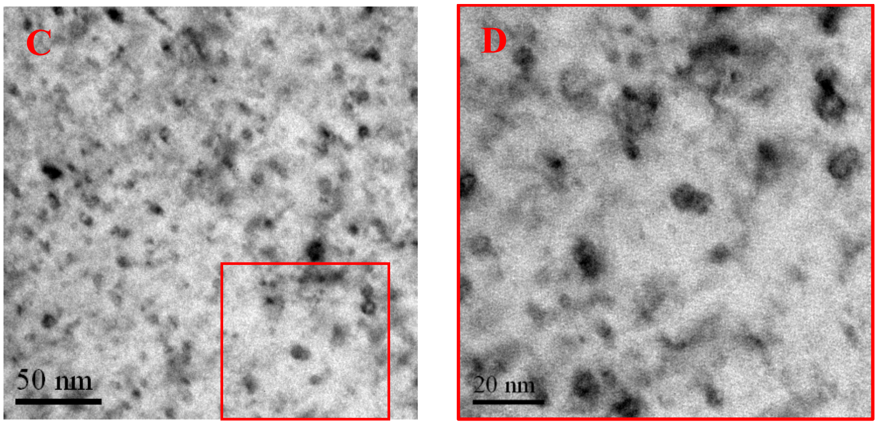

Figure 33 Microstructure comparison among 3C-SiC irradiated under different conditions. A is irradiated at 600 °C 0.3 dpa, B is sample irradiated at 600 °C 3 dpa, and C is sample irradiated at 900 °C 3 dpa. A, B and C share the same scale bar and the positions are all around radiation depth 1.5 μm. D is a zoomed-in image around the area within the red rectangle in C.

Chapter 4 discussed plastic deformation of thin 3C-SiC and the mechanism is the same as in metals, which is due to dislocation generation and movement. It is expected that radiation will affect thin 3C-SiC in the same way as metals, in which radiation causes hardening and embrittlement. That behavior is observed in the 600 °C 0.3 dpa and 600 °C 3 dpa samples. After radiation, point defects and their clusters act as obstacles pining and interacting with dislocations to impede dislocation movement, inducing hardening and increasing yield strength [48]. Based on Cottrell-Petch theory, the net effect of radiation is that yield strength increases much more than fracture strength, creating embrittlement [49]. This explains why resistance to cracking decreases after radiation at 600 °C. Moreover, Orowan stress, the critical stress to induced motion of dislocations through a field of obstacles, is proportional to the reciprocal of mean spacing between obstacles [48]. Therefore, higher defect concentration and smaller defect spacing will impede the dislocation movement more and cause more stress accumulation to the extent that cracking happens. This is consistent with the observation that 600 °C 3 dpa samples with higher defect concentration and smaller defect spacing (Figure 33B), are easier to fracture than 600 °C 0.3 dpa samples (Figure 33A). However, this theory does not explain the 900 °C 3 dpa samples, which have a high concentration of defects (Figure 33C and D) but no decreased resistance to cracking. The implication is that defect type as well as density influence the behavior.

Reduced radiation effects at higher temperature is observed also in the thermal conductivity of 3C-SiC. Price measured the thermal conductivity of neutron irradiated 3C-SiC at 2.7 dpa to 7.7 dpa at 550 °C and 1100 °C. The room-temperature thermal conductivity of the sample irradiated at 550 °C decreased by a factor of 9 with increasing fluence, while sample irradiated at 1100 °C had a reduction of only a factor of 3 [71]. Snead also showed that degradation of thermal conductivity of CVD polycrystalline 3C-SiC is more severe following at low temperature irradiation [72]. A summary of thermal conductivity degradation is in Ref [2] figure 23, showing room-temperature thermal conductivity of neutron irradiated 3C-SiC from 0.001 dpa to 10 dpa at temperatures from 80 °C to 800 °C. Before saturation, thermal conductivity degradation is severe at lower temperature and higher radiation fluence. The degradation of thermal conductivity due to radiation is called thermal defect resistance [113], which is defined as the difference between the reciprocal of irradiated and unirradiated thermal conductivity. Radiation-induced defects decrease the phonon mean free path [71], so thermal defect resistance increases after radiation. The thermal defect resistance reveals that when point defect concentration is high enough, thermal conductivity decrease is dominated by phonon scattering by point defects [114], especially the concentration of vacancies [113]. However, loops can be transparent to phonons except at high frequencies [113]. Therefore, radiation-induced degradation of thermal conductivity is reduced at higher temperatures.

Although phonons are not expected to play a key role in fracture, we speculate that loops may be "transparent" to dislocation created by deformation, instead of impeding their motion. The loops also may help relax stresses caused by other microstructure such as stacking faults and grain boundaries, so that motion of dislocations is not impeded by loops or stress will not be able to accumulate enough to cause fracture.

The results from *in situ* TEM nanoindentation tests only measure properties at small length scales, so they do not necessarily represent material properties at longer scales. As a result, macroscale mechanical properties such as fracture toughness, which represent the brittleness of bulk materials, are not necessarily to be comparable to the results from this study. As discussed in Chapter 2, it seems that there is a trend of fracture toughness in bulk 3C-SiC with radiation temperature: Below 400 °C, fracture toughness decreases slightly compared to as-synthesized material. From 300 °C to 1000 °C, fracture toughness increases with respect to as-synthesized material, and the increase grows larger with increasing temperature. At high temperature, there is almost no change of fracture toughness [2] [16] [55] [69]. If we assume that resistance to cracking is positively correlated to fracture toughness, the trend will be that fracture toughness decreases after radiated under 600 °C 0.3 dpa and 3 dpa, while increases back to as-synthesized fracture toughness after irradiated under 900 °C 3 dpa. Compared with literature results, this conclusion is opposite in intermediate temperature range, but consistent in high temperature range.

Chapter 6 *Ex situ* nanoindentation results

Elastic modulus and hardness on the same sample on both irradiated area and non-irradiated area were measured with respect to radiation depth on six sets of samples: 300 °C 0.6 dpa, 600 °C 0.3 dpa,600 °C 3 dpa, 900 °C 0.6 dpa, and 900 °C 3 dpa. After carefully correcting the projected contact areas using SEM measurement, there is no trend between modulus or hardness and radiation depth. We speculate that is due to the large effected area that contributes to the property values. Therefore, average of modulus and hardness of are calculated and used to represent the mechanical properties of the samples. Due to the limitation of the TriboIndenter accuracy, change smaller than 5% will be treated as fluctuation and systematic error, and will not be considered valid change. 3C-SiC irradiated under those conditions suggest reasonable change of modulus and hardness.

In general, modulus decreases after radiation without any specific relation to the temperature or radiation fluence, as shown in Figure 34A. The changing trend is partially consistent with the results in Ref [2], [15], and [115] that radiation reduces modulus with great reduction for lower temperature radiation. The reduction of modulus is caused by lattice expansion according to those researches. Hardness after radiation increases maximum 20% in this study, shown in Figure 34B, which is also consistent with the trend in Ref [2], [15], and [55]. Radiation induced hardening is expected due to the fact that defects will make dislocations motion more difficult.

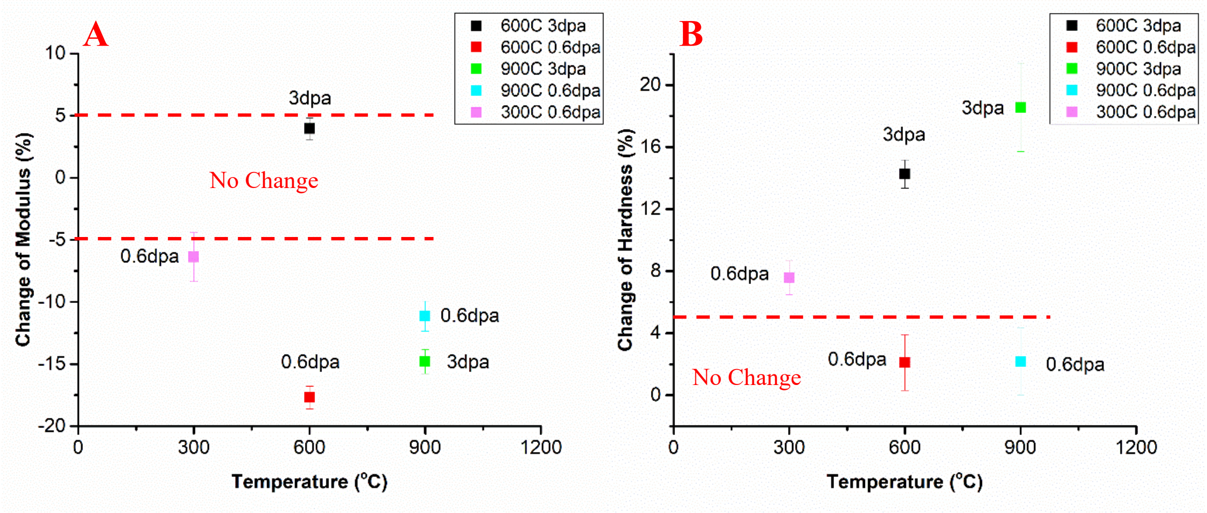

Figure 34 Change of elastic modulus and hardness results from *ex situ* nanoindentation tests

Chapter 7 Conclusions and Future Work

In situ nanoindentation tests in the TEM on thin 3C-SiC samples show that different behavior of thin 3C-SiC has been observed for samples with different thickness. Thinner samples are weaker and can fracture, while thicker samples can undergo plastic deformation during loading and sometimes exhibit plastic deformation recovery during unloading. Bend contours in TEM images provide visualization of the local elastic strain in the material. Plastic deformation is not caused by a change of crystal phase or amorphization of the sample, so we attribute it to nucleation and motion of dislocations. Dislocations are observed in small areas close to indents after indentation, but not during indentation. We speculate that the potential mechanism for plastic deformation recovery is related to disappearance of transient dislocations extension driven by retracted external stress during unloading. The behavior reported here emerges at certain scale size of thin 3C-SiC samples in our experiments. As a result, it does not reflect the behavior of bulk 3C-SiC, but it may be relevant to applications of SiC nanostructures in MEMS or NEMS devices and in thin SiC membranes or coatings.

In situ nanoindentation tests on three sets of 3C-SiC irradiated under different temperatures and fluences suggest a degradation of resistance of cracking after radiation based on the observation that 600 °C 0.3 dpa and 600 °C 3 dpa samples were easier to fracture and 3 dpa samples have characteristic long and straight crack paths. This trend can be explained by the increase of BSDs cluster density, which increase the impedance of dislocation motion. However, 900 °C 3 dpa samples deformed plastically under applied force, which is similar to as-synthesized 3C-SiC, and it indicates that temperature weakens the radiation effects. The defects in 900 °C 3 dpa samples are small loops that is completely different from defects in 600 °C samples. Therefore, we suspect that loops interact with dislocations differently from BSD clusters and they do not impede the dislocation motion, on the other hand, might help release stress so as to prevent fracture. This discover can be related to radiation induced embrittlement, but the results are contradictory to existing bulk material experimental results. Considering the size and geometry of this *in situ* study, difference from macroscale material results is expected. However, this study provides microscale experimental results to validate simulation and modelling to predict 3C-SiC in nuclear reactors in different scales.

Due to the arrival of new generation light water reactors, there is more and more need for investigation of promising nuclear materials to make that era to come sooner and mechanical properties are always significantly crucial for the operation of nuclear reactors. I propose several topics that might be interesting and important to explore in the future.

Regarding the goal of the project, there are more work that can be done. Firstly, using cluster dynamic simulation to validate irradiation-induced defect type, size and density distribution that have been observed in this study and figuring out the key factors that have real physical meanings behind to effect mechanical properties. Secondly, using phase field simulation to validate the fracture behavior with defects inside polycrystalline systems. Thirdly, using the key factors from cluster dynamic simulation as input to predict fracture behavior of 3C-SiC under radiation in microscale size.

Other parameters that might be important for the micromechanical properties of 3C-SiC under radiation can be investigated, for example, grain boundary and crystal orientation, pre-existing stacking faults and other special microstructures, amorphization, etc. *In situ* TEM nanoindentation tests can be also done on 3C-SiC with different sample geometry, for example samples having a notch inside or samples that are like levers hanging out with one side fixed to the bulk. *In situ* SEM nanoindentation tests can be done to connect *ex situ* nanoindentation tests and *in situ* TEM nanoindentation tests. It will provide a much large field of view to get results more comparable to results *ex situ* nanoindentation tests while showing the crack propagation during indentation.

Reference

1. Fisher GR, Barnes P (1990) Towards a unified view of polytypism in silicon carbide. Philos Mag B 61:217–236. https://doi.org/10.1080/13642819008205522
2. Snead LL, Nozawa T, Katoh Y, et al (2007) Handbook of SiC properties for fuel performance modeling. J Nucl Mater 371:329–377. https://doi.org/10.1016/j.jnucmat.2007.05.016
3. Ptb Shaffer B (1969) A Review of the Structure of Silicon Carbide. W. H
4. Goela JS, Burns LE, Taylor RL (1994) Transparent chemical vapor deposited β-SiC. Appl Phys Lett 64:131–133. https://doi.org/10.1063/1.111541
5. Olesinski RW, Abbaschian GJ (1984) The C−Si (Carbon-Silicon) system. In: Bulletin of Alloy Phase Diagrams. Springer US, pp 486–489
6. Philip G. Neudeck (2006) Silicon Carbide Technology. In: The VLSI Handbook. CRC Press LLC, pp 5-1-5–34
7. Choyke WJ, Matsunami H, Pensl G (2004) Silicon Carbide. Springer Berlin Heidelberg, Berlin, Heidelberg
8. J. B. CASADY RWJ (1996) Status of silicon carbide (SiC) as a wide-bandgap semiconductor for high-temperature applications: A review. Solid State Electron 39:1409–1422. https://doi.org/10.1016/0038-1101(96)00045-7
9. Michaud J-F, Portail M, Alquier D (2015) 3C-SiC — From Electronic to MEMS Devices. In: Advanced Silicon Carbide Devices and Processing. InTech, pp 33–60
10. Zorman CA, Mehregany M (2002) Silicon carbide for MEMS and NEMS - an overview. In: Proceedings of IEEE Sensors. IEEE, pp 1109–1114
11. KNIPPENBERG, F. W (1963) Growth phenomena in silicon carbide. Philips Res Rep

18:161–274

12. Levinshteĭn ME (Mikhail E, Rumyantsev SL, Shur M (2001) Properties of advanced semiconductor materials : GaN, AlN, InN, BN, SiC, SiGe. Wiley
13. Wang H, Singh RN, Goela JS (1995) Effects of Postdeposition Treatments on the Mechanical Properties of a Chemical-Vapor-Deposited Silicon Carbide. J Am Ceram Soc 78:2437–2442. https://doi.org/10.1111/j.1151-2916.1995.tb08682.x
14. Yavuz BO, Tressler RE (1992) High temperature mechanical behavior of a chemically vapor deposited beta silicon carbide. Ceram Int 18:19–26. https://doi.org/10.1016/0272-8842(92)90057-K
15. Katoh Y, Snead LL (2005) Mechanical Properties of Cubic Silicon Carbide after Neutron Irradiation at Elevated Temperatures. J ASTM Int 2:12377. https://doi.org/10.1520/JAI12377
16. Osborne MC, Hay JC, Snead LL, Steiner D (1999) Mechanical- and Physical-Property Changes of Neutron-Irradiated Chemical-Vapor-Deposited Silicon Carbide. John Wiley & Sons, Ltd (10.1111)
17. Reddy JD, Volinsky AA, Frewin CL, et al (2007) Mechanical Properties of 3C-SiC Films for MEMS Applications. MRS Proc 1049:1049-AA03-06. https://doi.org/10.1557/PROC-1049-AA03-06
18. Locke C, Kravchenko G, Waters P, et al (2009) 3C-SiC Films on Si for MEMS Applications: Mechanical Properties. Mater Sci Forum 615–617:633–636. https://doi.org/10.4028/www.scientific.net/MSF.615-617.633
19. Tong L, Mehregany M, Matus LG (1992) Mechanical properties of 3C silicon carbide. Appl Phys Lett 60:2992–2994. https://doi.org/10.1063/1.106786

20. Jackson KM, Edwards RL, Dirras GF, Sharpe WN (2001) Mechanical Properties of Thin Film Silicon Carbide. MRS Proc 687:B6.3. https://doi.org/10.1557/PROC-687-B6.3
21. Jackson KM (2005) Fracture strength, elastic modulus and Poisson's ratio of polycrystalline 3C thin-film silicon carbide found by microsample tensile testing. Sensors Actuators A Phys 125:34–40. https://doi.org/10.1016/J.SNA.2004.10.008
22. Shin C, Jin H-H, Kim W-J, Park J-Y (2012) Mechanical Properties and Deformation of Cubic Silicon Carbide Micropillars in Compression at Room Temperature. J Am Ceram Soc 95:2944–2950. https://doi.org/10.1111/j.1551-2916.2012.05346.x
23. Milman YV, Chugunova SI, Goncharova IV, et al (1999) Temperature dependence of hardness in silicon–carbide ceramics with different porosity. Int J Refract Met Hard Mater 17:361–368. https://doi.org/10.1016/S0263-4368(99)00022-0
24. Merkel I, Messerschmidt U (1992) Fracture toughness of sintered SiC ceramics: a comparison between different methods. Mater Sci Eng A 151:131–135. https://doi.org/10.1016/0921-5093(92)90200-K
25. JORGENSEN PJ, WADSWORTH ME, CUTLER IB (1959) Oxidation of Silicon Carbide. J Am Ceram Soc 42:613–616. https://doi.org/10.1111/j.1151-2916.1959.tb13582.x
26. Narushima T, Goto T, Hirai T, Iguchi Y (1997) High-Temperature Oxidation of Silicon Carbide and Silicon Nitride. Mater Trans JIM 38:821–835. https://doi.org/10.2320/matertrans1989.38.821
27. Zorman CA, Parro RJ (2008) Micro- and nanomechanical structures for silicon carbide MEMS and NEMS. WILEY-VCH Verlag
28. Chang W, Zorman C (2008) Determination of Young's moduli of 3C (110) single-crystal

and (111) polycrystalline silicon carbide from operating frequencies. J Mater Sci 43:4512–4517. https://doi.org/10.1007/s10853-008-2648-4

29. Placidi M, Godignon P, Mestres N, et al (2008) Fabrication of monocrystalline 3C–SiC resonators for MHz frequency sensors applications. Sensors Actuators B Chem 133:276–280. https://doi.org/10.1016/J.SNB.2007.07.148
30. Boubekri R, Cambril E, Couraud L, et al (2014) Electrothermally driven high-frequency piezoresistive SiC cantilevers for dynamic atomic force microscopy. J Appl Phys 116:054304. https://doi.org/10.1063/1.4891833
31. Mehregany M (2013) Advances in silicon carbide micro- and nano-electro-mechanical systems fabrication technology and applications. In: 2013 Transducers & Eurosensors XXVII: The 17th International Conference on Solid-State Sensors, Actuators and Microsystems (TRANSDUCERS & EUROSENSORS XXVII). IEEE, pp 2397–2402
32. M. Placidia, P. Godignona, N. Mestresa, G. Abadalb,G.Ferroc, A. Leycurasd TC (2008) Fabrication of monocrystalline 3C–SiC resonators for MHz frequency sensors applications. Sensors Actuators B Chem 133:276–280. https://doi.org/10.1016/J.SNB.2007.07.148
33. Mehregany M, Zorman CA (2004) Silicon carbide micro- and nanoelectromechanical systems. In: Maher MA, Jakubczak JF (eds) Proc. of SPIE. International Society for Optics and Photonics, pp 1–7
34. Olander D (2009) Nuclear fuels – Present and future. J Nucl Mater 389:1–22. https://doi.org/10.1016/j.jnucmat.2009.01.297
35. Idaho National Laboratory (2010) Summary for the Next Generation Nuclear Plant Project In Review. INL/EXT-10-19142

36. Hosemann P, Martos JN, Frazer D, et al (2013) Mechanical characteristics of SiC coating layer in TRISO fuel particles. J Nucl Mater 442:133–142. https://doi.org/10.1016/j.jnucmat.2013.08.041

37. Rohbeck, Nadia PX (2016) Evaluation of the mechanical performance of silicon carbide in TRISO fuel at high temperatures. Nucl Eng Des 306:52–58. https://doi.org/10.1016/J.NUCENGDES.2016.05.040

38. Powers JJ, Wirth BD (2010) A review of TRISO fuel performance models. J Nucl Mater 405:74–82. https://doi.org/10.1016/J.JNUCMAT.2010.07.030

39. Davis BC, Ward L, Butt DP, et al (2016) Fracture strength and principal stress fields during crush testing of the SiC layer in TRISO-coated fuel particles. J Nucl Mater 477:263–272. https://doi.org/10.1016/j.jnucmat.2016.05.018

40. Snead LL, Nozawa T, Ferraris M, et al (2011) Silicon carbide composites as fusion power reactor structural materials. J Nucl Mater 417:330–339. https://doi.org/10.1016/j.jnucmat.2011.03.005

41. Katoh Y, Snead LLL, Henager CHH, et al (2007) Current status and critical issues for development of SiC composites for fusion applications. J Nucl Mater 367:659–671. https://doi.org/10.1016/j.jnucmat.2007.03.032

42. Katoh Y, Snead LL, Szlufarska I, Weber WJ (2012) Radiation effects in SiC for nuclear structural applications. Curr Opin Solid State Mater Sci 16:143–152. https://doi.org/10.1016/j.cossms.2012.03.005

43. Giancarli L, B HG, C SN, et al (2002) Progress in blanket designs using SiC/SiC composites. Fusion Eng Des 61–62:307–318. https://doi.org/10.1016/S0920-3796(02)00213-2

44. J.D. Hales, S.R. Novascone, B.W. Spencer, R.L. Williamson, G. Pastore DMP (2014) Verification of the BISON fuel performance code. Ann Nucl Energy 71:81–90. https://doi.org/10.1016/J.ANUCENE.2014.03.027

45. J.D. Hales, R.L. Williamson, S.R. Novascone, D.M. Perez, B.W. Spencer GP (2013) Multidimensional multiphysics simulation of TRISO particle fuel. J Nucl Mater 443:531–543. https://doi.org/10.1016/J.JNUCMAT.2013.07.070

46. Liu C, He L, Zhai Y, et al (2017) Evolution of small defect clusters in ion-irradiated 3C-SiC: Combined cluster dynamics modeling and experimental study. Acta Mater 125:377–389. https://doi.org/10.1016/j.actamat.2016.12.020

47. Tyburska-Püschel B, Zhai Y, He L, et al (2016) Size distribution of black spot defects and their contribution to swelling in irradiated SiC. J Nucl Mater J 476:132–139. https://doi.org/10.1016/j.jnucmat.2016.04.044

48. Olander D, Motta A, Wirth B (2017) Light Water Reactor Materials, 1st ed. American Nuclear Society

49. Was GS (2016) Fundamentals of Radiation Materials Science, Second. Springer, New York

50. Wang X, Jamison L, Sridharan K, et al (2015) Evidence for cascade overlap and grain boundary enhanced amorphization in silicon carbide irradiated with Kr ions. Acta Mater 99:7–15. https://doi.org/10.1016/j.actamat.2015.07.070

51. Bayu Aji LB, Wallace JB, Kucheyev SO (2017) Effects of collision cascade density on radiation defect dynamics in 3C-SiC. Sci Rep 7:44703. https://doi.org/10.1038/srep44703

52. Weber WJ, Gao F (2010) Irradiation-induced defect clustering and amorphization in silicon carbide. J Mater Res 25:2349–2353. https://doi.org/10.1557/jmr.2010.0292

53. Katoh Y, Hashimoto N, Kondo S, et al (2006) Microstructural development in cubic silicon carbide during irradiation at elevated temperatures. J Nucl Mater 351:228–240. https://doi.org/10.1016/J.JNUCMAT.2006.02.007

54. Malherbe JB (2013) Diffusion of fission products and radiation damage in SiC. J Phys D Appl Phys 46:473001. https://doi.org/10.1088/0022-3727/46/47/473001

55. Snead LL, Katoh Y, Nozawa T (2012) Radiation Effects in SiC and SiC–SiC. Compr Nucl Mater 215–240. https://doi.org/10.1016/B978-0-08-056033-5.00093-8

56. He L, Jiang H, Zhai Y, et al (2015) Atomic Resolution Imaging of Black Spot Defects in Ion Irradiated Silicon Carbide. Microsc Microanal 21:1337–1338. https://doi.org/10.1017/s1431927615007473

57. Zinkle SJ, Seitzman LE, Wolfer WG, et al (1987) I. Energy calculations for pure metals. Philos Mag A Phys Condens Matter, Struct Defects Mech Prop 55:111–125. https://doi.org/10.1080/01418618708209803

58. Lin, Yan-Ru, Ching-Shun Ku C-YH, Lin Y-R, Ku C-S, et al (2015) Irradiation-induced microstructural evolution and swelling of 3C-SiC. J Nucl Mater 459:276–283. https://doi.org/10.1016/J.JNUCMAT.2015.01.040

59. D.J. Sprouster, T. Koyanagi ED, Sprouster DJ, Koyanagi T, et al (2017) Microstructural evolution of neutron irradiated 3C-SiC. Scr Mater 137:132–136. https://doi.org/10.1016/J.SCRIPTAMAT.2017.02.030

60. Lin YR, Chen LG, Hsieh CY, et al (2017) Atomic Configuration of Point Defect Clusters in Ion-Irradiated Silicon Carbide. Sci Rep 7:14635. https://doi.org/10.1038/s41598-017-15037-w

61. Xi J, Zhang P, He C, et al (2015) The role of point defects in the swelling and elastic

modulus of irradiated cubic silicon carbide. Nucl Instruments Methods Phys Res Sect B Beam Interact with Mater Atoms 356–357:62–68. https://doi.org/10.1016/J.NIMB.2015.04.059

62. Senor D., Youngblood G., Greenwood L., et al (2003) Defect structure and evolution in silicon carbide irradiated to 1 dpa-SiC at 1100 °C. J Nucl Mater 317:145–159. https://doi.org/10.1016/S0022-3115(03)00077-1
63. Kondo S, Katoh Y, Snead LL (2009) Cavity swelling and dislocation evolution in SiC at very high temperatures. J Nucl Mater 386–388:222–226. https://doi.org/10.1016/J.JNUCMAT.2008.12.095
64. Sprouster DJ, Koyanagi T, Dooryhee E, et al (2018) Reprint of: Microstructural evolution of neutron irradiated 3C-SiC. Scr Mater 143:176–180. https://doi.org/10.1016/J.SCRIPTAMAT.2017.09.034
65. T. Yano, H. Miyazaki, M. Akiyoshi, T. Iseki (1998) X-ray diffractometry and high-resolution electron microscopy of neutron-irradiated SiC to a fluence of 1.9×1027 n/m2. J Nucl Mater 253:78–86. https://doi.org/10.1016/S0022-3115(97)00331-0
66. Nogami S, Hasegawa A, Snead LL (2002) Indentation fracture toughness of neutron irradiated silicon carbide. J Nucl Mater 307–311:1163–1167. https://doi.org/10.1016/S0022-3115(02)01055-3
67. Snead LL, Hay JC (1999) Neutron irradiation induced amorphization of silicon carbide. J Nucl Mater 273:213–220. https://doi.org/10.1016/S0022-3115(99)00023-9
68. Evans AG (1979) FRACTURE TOUGHNESS: THE ROLE OF INDENTATION TECHNIQUES. ASTM Spec. Tech. Publ. 112–135
69. Park KH, Kondo S, Katoh Y, Kohyama A (2003) Mechanical Properties of β-SiC After

Si- and Dual Si + He-Ion Irradiation at Various Temperatures. Fusion Sci Technol 44:455–459. https://doi.org/10.13182/FST03-A377

70. Clinard FW, Hurley GF, Youngman RA, Hobbs LW (1985) The effect of elevated-temperature neutron irradiation on fracture toughness of ceramics. J Nucl Mater 133–134:701–704. https://doi.org/10.1016/0022-3115(85)90239-9

71. R.J. Price (1973) Thermal conductivity of neutron-irradiated pyrolytic β-silicon carbide. J Nucl Mater 46:268–272. https://doi.org/10.1016/0022-3115(73)90041-X

72. Snead L. (2004) Limits on irradiation-induced thermal conductivity and electrical resistivity in silicon carbide materials. J Nucl Mater 329–333:524–529. https://doi.org/10.1016/J.JNUCMAT.2004.04.294

73. Taheri ML, Stach EA, Arslan I, et al (2016) Current status and future directions for in situ transmission electron microscopy. Ultramicroscopy 170:86–95

74. Li J, Johnson G, Zhang S, Su D (2019) In Situ Transmission Electron Microscopy for Energy Applications. Joule 3:4–8

75. Williamson MJ, Tromp RM, Vereecken PM, et al (2003) Dynamic microscopy of nanoscale cluster growth at the solid-liquid interface. Nat. Mater. 2:532–536

76. Chen Q, Smith JM, Park J, et al (2013) 3D motion of DNA-Au nanoconjugates in graphene liquid cell electron microscopy. Nano Lett 13:4556–4561. https://doi.org/10.1021/nl402694n

77. Textor M, De Jonge N (2018) Strategies for Preparing Graphene Liquid Cells for Transmission Electron Microscopy. Nano Lett. 18:3313–3321

78. Saka H, Kamino T, Ara S, Sasaki K (2008) In Situ Heating Transmission Electron Microscopy . MRS Bull 33:93–100. https://doi.org/10.1557/mrs2008.21

79. Wall MA, Dahmen U (1998) An in situ nanoindentation specimen holder for a high voltage transmission electron microscope. Microsc Res Tech 42:248–254. https://doi.org/10.1002/(SICI)1097-0029(19980915)42:4<248::AID-JEMT3>3.0.CO;2-M

80. Gammer C, Kacher J, Czarnik C, et al (2016) Local and transient nanoscale strain mapping during in situ deformation. Appl Phys Lett 109:081906. https://doi.org/10.1063/1.4961683

81. Wang ZL (2003) New developments in transmission electron microscopy for nanotechnology. Adv. Mater. 15:1497–1514

82. Warren OL, Shan Z, Syed Asif SA, et al (2007) In situ nanoindentation in the TEM. Materialstoday 10:59–60

83. Stach EA, Freeman T, Minor AM, et al (2001) Development of a Nanoindenter for In Situ Transmission Electron Microscopy. Microsc Microanal 7:507–517. https://doi.org/10.1007/s10005-001-0012-4

84. Wang X, Mao S, Zhang J, et al (2017) MEMS device for quantitative in situ mechanical testing in electron microscope. Micromachines 8:. https://doi.org/10.3390/mi8020031

85. Fischer-Cripps AC (2011) Nanoindentation. In: Mechanical Engineering Series, 3rd editio. Springer New York, New York, NY

86. Zhang P, Wang Z, Perepezko JH, Voyles PM (2016) Elastic and inelastic mean free paths of 200 keV electrons in metallic glasses. Ultramicroscopy 171:89–95. https://doi.org/10.1016/j.ultramic.2016.09.005

87. Chen B, Wang J, Zhu Y, et al (2014) Deformation-induced phase transformation in 4H–SiC nanopillars. Acta Mater 80:392–399. https://doi.org/10.1016/j.actamat.2014.07.055

88. Kiani S, Leung KWK, Radmilovic V, et al (2014) Dislocation glide-controlled room-

temperature plasticity in 6H-SiC single crystals. Acta Mater 80:400–406. https://doi.org/10.1016/j.actamat.2014.07.066

89. Zhang Y, Han X, Zheng K, et al (2007) Direct Observation of Super-Plasticity of Beta-SiC Nanowires at Low Temperature. Adv Funct Mater 17:3435–3440. https://doi.org/10.1002/adfm.200700162

90. Wang J, Lu C, Wang Q, et al (2011) Understanding large plastic deformation of SiC nanowires at room temperature. EPL (Europhysics Lett 95:63003. https://doi.org/10.1209/0295-5075/95/63003

91. Williams DB, Carter CB (2009) Transmission Electron Microscopy, Second. Springer US, Boston, MA

92. CALVIÉ E, JOLY-POTTUZ L, ESNOUF C, et al (2013) A global investigation into *in situ* nanoindentation experiments on zirconia: from the sample geometry optimization to the stress nanolocalization using convergent beam electron diffraction. J Microsc 249:99–110. https://doi.org/10.1111/j.1365-2818.2012.03689.x

93. Minor AAM, Lilleodden ETE, JIN yô M, et al (2005) Room temperature dislocation plasticity in silicon. Philos Mag 85:323–330. https://doi.org/10.1080/14786430412331315680

94. Carlton CE, Ferreira PJ (2012) In situ TEM nanoindentation of nanoparticles. Micron 43:1134–1139. https://doi.org/10.1016/j.micron.2012.03.002

95. Liu HH, Duan XF, Xu Q, Liu B-G (2008) Study of strained-silicon channel metal-oxide-semiconductor field effect transistors by large angle convergent-beam electron diffraction. Ultramicroscopy 108:816–820. https://doi.org/10.1016/j.ultramic.2008.01.002

96. Hÿtch MJ, Minor AM (2014) Observing and measuring strain in nanostructures and

devices with transmission electron microscopy. MRS Bull 39:138–146. https://doi.org/10.1557/mrs.2014.4

97. Meyers MA, Chawla KK (2008) Fracture: Macroscopic Aspects. In: Mechanical Behavior of Materials, 2nd ed. Cambridge University Press, Cambridge, pp 326–380

98. Kang W, Saif MTA (2013) In Situ Study of Size and Temperature Dependent Brittle-to-Ductile Transition in Single Crystal Silicon. Adv Funct Mater 23:713–719. https://doi.org/10.1002/adfm.201201992

99. Gumbsch P, Taeri-Baghbadrani S, Brunner D, et al (2001) Plasticity and an Inverse Brittle-to-Ductile Transition in Strontium Titanate. Phys Rev Lett 87:085505. https://doi.org/10.1103/PhysRevLett.87.085505

100. Keonwook Kang WC (2010) Size and temperature effects on the fracture mechanisms of silicon nanowires: Molecular dynamics simulations. Int J Plast 26:1387–1401. https://doi.org/10.1016/J.IJPLAS.2010.02.001

101. Szlufarska I, Kalia RK, Nakano A, Vashishta P (2004) Nanoindentation-induced amorphization in silicon carbide. Appl Phys Lett 85:378–380. https://doi.org/10.1063/1.1774252

102. Han XD, Zhang YF, Zheng K, et al (2006) Low-Temperature in Situ Large Strain Plasticity of Ceramic SiC Nanowires and Its Atomic-Scale Mechanism. Nano Lett 7:452–457. https://doi.org/10.1021/NL0627689

103. Vlaskina SI, Mishinova GN, Vlaskin VI, et al (2011) 3C-6H transformation in heated cubic silicon carbide 3C-SiC. Semicond Physics, Quantum Electron Optoelectron 14:432–436

104. Deva Reddy J (2008) Mechanical properties of Silicon Carbide (SiC) thin films.

University of South Florida

105. Fu XA, Dunning JL, Zorman CA, Mehregany M (2005) Measurement of residual stress and elastic modulus of polycrystalline 3C-SiC films deposited by low-pressure chemical vapor deposition. Thin Solid Films 492:195–202. https://doi.org/10.1016/j.tsf.2005.07.236

106. Li X, Wei Y, Yang W, Gao H (2009) Competing grain-boundary- and dislocation-mediated mechanisms in plastic strain recovery in nanocrystalline aluminum. Proc Natl Acad Sci U S A 106:16108–13. https://doi.org/10.1073/pnas.0901765106

107. Rajagopalan J, Han JH, Saif MTA (2007) Plastic Deformation Recovery in Freestanding Nanocrystalline Aluminum and Gold Thin Films. Science (80-) 315:

108. Kingstedt OTT, Eftink BPP, Robertson IMM, Lambros J (2016) Inelastic strain recovery of a dynamically deformed unidirectional AgeCu eutectic alloy. Acta Mater 113:239–300. https://doi.org/10.1016/j.actamat.2016.04.043

109. Eftink BP, Li A, Szlufarska I, Robertson IM (2016) Interface mediated mechanisms of plastic strain recovery in a AgCu alloy. Acta Mater 117:111–121. https://doi.org/10.1016/j.actamat.2016.07.010

110. Li R, Chew HB (2014) Deformation twinning and plastic recovery in Cu/Ag nanolayers under uniaxial tensile straining. Philos Mag Lett 94:260–268. https://doi.org/10.1080/09500839.2014.893063

111. Wei X, Kysar JW (2011) Residual plastic strain recovery driven by grain boundary diffusion in nanocrystalline thin films. Acta Mater 59:3937–3945. https://doi.org/10.1016/J.ACTAMAT.2011.03.019

112. Hull D, Bacon DJ (2011) Origin and Multiplication of Dislocations. In: Introduction to Dislocations, 5th ed. Elsevier, pp 157–169

113. Snead LL, Zinkle SJ, White DP (2005) Thermal conductivity degradation of ceramic materials due to low temperature, low dose neutron irradiation. J Nucl Mater 340:187–202. https://doi.org/10.1016/j.jnucmat.2004.11.009

114. Crocombette JP, Proville L (2011) Thermal conductivity degradation induced by point defects in irradiated silicon carbide. Appl Phys Lett 98:. https://doi.org/10.1063/1.3589358

115. Katoh Y, Snead LL, Nozawa T, et al (2010) Thermophysical and mechanical properties of near-stoichiometric fiber CVI SiC/SiC composites after neutron irradiation at elevated temperatures. J Nucl Mater 403:48–61. https://doi.org/10.1016/j.jnucmat.2010.06.002